CHAPTER

6

Multimode Multiline Thru-Line-Reflect Calibration

6.1 Introduction

Low loss waveguides have for long been related with multimode propagation since in most waveguides the minimum of the attenuation constant is achieved for higher-order modes. However, measurements, to the author knowledge, have not been carried out accurately since no procedure was available at the time they developed those transmission media. In 1998, a new calibration method was published [1] that is based on the TRL calibration but it can take into account several modes. The topic arose some interest and other works were included in the literature [2, 3, 4, 5]. However, neither of them are accurate enough to measure transmission media since they do only use as standards a thru and a line, making the method narrow band and not accurate since the line cannot be optimal for both modes at the same time. Therefore, along this chapter, the propagation constant estimation based on the CPD MTRL, detailed in Chapter 3, has been extended to a Multimode

MTRL (MMTRL) method. Also, the completion of the procedure to be used as a calibration procedure has been developed.

So, first of all, the MMTRL procedure to estimate the propagation constant of any transmission medium is described in Section 6.2. Then, using this technique the measurement of the propagation constant of a WR-90 waveguide filled of FOREX in a band in which several modes can propagate is shown in Section 6.3. Section 6.4 and Section 6.5 give the details of the MMTRL calibration implementation, as well as the simulation results for several filters. Finally, Section 6.6 gives the measured results for the calibration procedure. The chapter ends with some conclusions given in Section 6.7.

6.2 Multimode Multiline TRL Propagation Constant Calculation

From Chapter 3 we can write that, when measuring with a VNA, the measured wave-chain (or wave-cascading) matrix, with $\mathbf{X}$ and $\mathbf{Y}$ representing the VNA non-idealities and with $\mathbf{T}^i$ the transfer matrix of the i-th measured line, can be expressed as:

$$\mathbf{M}^i = \begin{bmatrix} x_{11} & x_{12} \\ x_{21} & x_{22} \end{bmatrix} A \begin{bmatrix} \alpha & 0 \\ 0 & 1 \end{bmatrix} \mathbf{P} \begin{bmatrix} e^{-\gamma l_i} & 0 \\ 0 & e^{+\gamma l_i} \end{bmatrix} \mathbf{P} B \begin{bmatrix} \beta & 0 \\ 0 & 1 \end{bmatrix} \begin{bmatrix} y_{11} & y_{12} \\ y_{21} & y_{22} \end{bmatrix} \tag{6.1}$$

where $\mathbf{P}$ is a permutation matrix and A, α, B and β are unknown scalar values. If instead of one mode, two modes were considered, then,

$$\begin{aligned} \mathbf{M}^i = & \begin{bmatrix} x_{11} & x_{12} & x_{13} & x_{14} \\ x_{21} & x_{22} & x_{23} & x_{24} \\ x_{31} & x_{32} & x_{33} & x_{34} \\ x_{41} & x_{42} & x_{43} & x_{44} \end{bmatrix} A \begin{bmatrix} \alpha & 0 & 0 & 0 \\ 0 & \beta & 0 & 0 \\ 0 & 0 & \xi & 0 \\ 0 & 0 & 0 & 1 \end{bmatrix} \mathbf{P} \\ & \begin{bmatrix} e^{-\gamma_1 l_i} & 0 & 0 & 0 \\ 0 & e^{-\gamma_2 l_i} & 0 & 0 \\ 0 & 0 & e^{+\gamma_1 l_i} & 0 \\ 0 & 0 & 0 & e^{+\gamma_2 l_i} \end{bmatrix} \mathbf{P} B \begin{bmatrix} \iota & 0 & 0 & 0 \\ 0 & \kappa & 0 & 0 \\ 0 & 0 & \nu & 0 \\ 0 & 0 & 0 & 1 \end{bmatrix} \begin{bmatrix} y_{11} & y_{12} & y_{13} & y_{14} \\ y_{21} & y_{22} & y_{23} & y_{24} \\ y_{31} & y_{32} & y_{33} & y_{34} \\ y_{41} & y_{42} & y_{43} & y_{44} \end{bmatrix} \end{aligned} \tag{6.2}$$

And if N modes were considered the measurement will be expressed as:

$$\mathbf{M}^i = \begin{bmatrix} x_{1,1} & x_{1,2} & \cdots & x_{1,2N} \\ x_{2,1} & x_{2,2} & \cdots & x_{2,2N} \\ \vdots & \vdots & \ddots & \vdots \\ x_{2N,1} & x_{2N,2} & \cdots & x_{2N,2N} \end{bmatrix} A \begin{bmatrix} \alpha & 0 & \cdots & 0 \\ 0 & \beta & \cdots & 0 \\ \vdots & \vdots & \ddots & \vdots \\ 0 & 0 & \cdots & 1 \end{bmatrix} \mathbf{P} \begin{bmatrix} e^{-\gamma_1 l_i} & 0 & \cdots & 0 \\ 0 & e^{-\gamma_2 l_i} & \cdots & 0 \\ \vdots & \vdots & \ddots & \vdots \\ 0 & 0 & \cdots & e^{+\gamma_N l_i} \end{bmatrix} \mathbf{P} B \begin{bmatrix} \iota & 0 & \cdots & 0 \\ 0 & \kappa & \cdots & 0 \\ \vdots & \vdots & \ddots & \vdots \\ 0 & 0 & \cdots & 1 \end{bmatrix} \begin{bmatrix} y_{1,1} & y_{1,2} & \cdots & y_{1,2N} \\ y_{2,1} & y_{2,2} & \cdots & y_{2,2N} \\ \vdots & \vdots & \ddots & \vdots \\ y_{2N,1} & y_{2N,2} & \cdots & y_{2N,2N} \end{bmatrix} \tag{6.3}$$

With some work, the previous expression can be rewritten in a vectorial form to get an analogous expression to the one presented for the monomode case. The unknown scalars are taken into account through a scaling factor λ_i:

$$
\begin{aligned}
\mathbf{M}^i = \lambda_1 &\begin{bmatrix} x_{1,1} \\ x_{2,1} \\ \vdots \\ x_{2N,1} \end{bmatrix} \begin{bmatrix} y_{1,1} & y_{1,2} & \cdots & y_{1,2N} \end{bmatrix} e^{\mp\gamma_1 l_i} + \\
+\lambda_2 &\begin{bmatrix} x_{1,2} \\ x_{2,2} \\ \vdots \\ x_{2N,2} \end{bmatrix} \begin{bmatrix} y_{2,1} & y_{2,2} & \cdots & y_{2,2N} \end{bmatrix} e^{\mp\gamma_2 l_i} + \\
&\qquad\qquad\qquad\qquad\qquad\qquad\qquad\qquad + \cdots + \\
+\lambda_N &\begin{bmatrix} x_{1,N} \\ x_{2,N} \\ \vdots \\ x_{2N,N} \end{bmatrix} \begin{bmatrix} y_{N,1} & y_{N,2} & \cdots & y_{N,2N} \end{bmatrix} e^{\mp\gamma_N l_i} + \\
+\lambda_{N+1} &\begin{bmatrix} x_{1,N+1} \\ x_{2,N+1} \\ \vdots \\ x_{2N,N+1} \end{bmatrix} \begin{bmatrix} y_{N+1,1} & y_{N+1,2} & \cdots & y_{N+1,2N} \end{bmatrix} e^{\pm\gamma_1 l_i} + \\
&\qquad\qquad\qquad\qquad\qquad\qquad\qquad\qquad + \cdots + \\
+\lambda_{2N} &\begin{bmatrix} x_{1,2N} \\ x_{2,2N} \\ \vdots \\ x_{2N,2N} \end{bmatrix} \begin{bmatrix} y_{2N,1} & y_{2N,2} & \cdots & y_{2N,2N} \end{bmatrix} e^{\pm\gamma_N l_i}
\end{aligned}
\tag{6.4}
$$

or

$$
\begin{aligned}
\mathbf{M}^i = &\lambda_1 e^{\mp\gamma_1 l_i} \mathbf{a} \odot \mathbf{b} + \lambda_2 e^{\mp\gamma_2 l_i} \mathbf{c} \odot \mathbf{d} + \cdots \\
&+ \lambda_N e^{\mp\gamma_N l_i} \mathbf{g} \odot \mathbf{h} + \lambda_{N+1} e^{\pm\gamma_1 l_i} \mathbf{m} \odot \mathbf{n} + \cdots \\
&+ \lambda_{2N} e^{\pm\gamma_N l_i} \mathbf{p} \odot \mathbf{q}
\end{aligned}
\tag{6.5}
$$

where $\odot$ denotes the outer product between two column vectors $\mathbf{a} \odot \mathbf{b} = \mathbf{a}\mathbf{b}^T$ being the superindex T the transpose operation. Then, taking into account all lines simultaneously it can be written:

$$\begin{aligned}\mathcal{T} =&\lambda_1 \mathbf{a} \odot \mathbf{b} \odot \mathbf{e}_1 + \lambda_2 \mathbf{c} \odot \mathbf{d} \odot \mathbf{e}_2 + \cdots \\ &+ \lambda_N \mathbf{g} \odot \mathbf{h} \odot \mathbf{e}_N + \lambda_{N+1} \mathbf{m} \odot \mathbf{n} \odot \mathbf{e}_{N+1} + \cdots \\ &+ \lambda_{2N} \mathbf{p} \odot \mathbf{q} \odot \mathbf{e}_{2N}\end{aligned} \tag{6.6}$$

where $\mathbf{e}_i$ contains the propagation constants of the modes propagationg in the k lines considered in the measurement process.

We can define the factor matrices:

$$\begin{aligned}\dot{\mathbf{X}} &= \begin{bmatrix}\mathbf{a} & \mathbf{c} & \cdots & \mathbf{g} & \mathbf{m} & \cdots & \mathbf{p}\end{bmatrix} = \begin{bmatrix} x_{1,1} & x_{1,2} & \cdots & x_{1,2N} \\ x_{2,1} & x_{2,2} & \cdots & x_{2,2N} \\ \vdots & \vdots & \ddots & \vdots \\ x_{2N,1} & x_{2N,2} & \cdots & x_{2N,2N} \end{bmatrix} \\ \dot{\mathbf{Y}}^T &= \begin{bmatrix}\mathbf{b} & \mathbf{d} & \cdots & \mathbf{h} & \mathbf{n} & \cdots & \mathbf{q}\end{bmatrix}^T = \begin{bmatrix} y_{1,1} & y_{1,2} & \cdots & y_{1,2N} \\ y_{2,1} & y_{2,2} & \cdots & y_{2,2N} \\ \vdots & \vdots & \ddots & \vdots \\ y_{2N,1} & y_{2N,2} & \cdots & y_{2N,2N} \end{bmatrix}\end{aligned} \tag{6.7}$$

And,

$$\mathbf{D} = \begin{bmatrix} e^{\mp\gamma_1 l_1} & e^{\mp\gamma_2 l_1} & \ldots & e^{\mp\gamma_N l_1} & e^{\pm\gamma_1 l_1} & e^{\pm\gamma_2 l_1} & \ldots & e^{\pm\gamma_N l_1} \\ e^{\mp\gamma_1 l_2} & e^{\mp\gamma_2 l_2} & \ldots & e^{\mp\gamma_N l_2} & e^{\pm\gamma_1 l_2} & e^{\pm\gamma_2 l_2} & \ldots & e^{\pm\gamma_N l_2} \\ e^{\mp\gamma_1 l_3} & e^{\mp\gamma_2 l_3} & \ldots & e^{\mp\gamma_N l_3} & e^{\pm\gamma_1 l_3} & e^{\pm\gamma_2 l_3} & \ldots & e^{\pm\gamma_N l_3} \\ \vdots & \vdots & & & \ddots & & & \vdots \\ e^{\mp\gamma_1 l_k} & e^{\mp\gamma_2 l_k} & \ldots & e^{\mp\gamma_N l_k} & e^{\pm\gamma_1 l_k} & e^{\pm\gamma_2 l_k} & \ldots & e^{\pm\gamma_N l_k} \end{bmatrix} \tag{6.8}$$

The $\mathbf{D}$ matrix is written this way to show that in each column of $\mathbf{D}$ we can obtain either a positive or a negative exponential, as a result of the presence of the permutation matrix $\mathbf{P}$ in (6.3). But it is not possible that both types of exponentials or modes are mixed in the same column. In short, the permutation $\mathbf{P}$ implies that columns in $\mathbf{D}$, as a whole, interchange positions as it can be deduced from (6.3). Therefore, the mode identification task in $\mathbf{D}$ does not only include the differentiation between the modes propagating forward and backward as in the monomode case, but it is also necessary to differentiate between modes with a different propagation constant.

Let us define $\boldsymbol{\lambda} = \begin{bmatrix}\lambda_1 & \lambda_2 & \cdots & \lambda_N & \lambda_{N+1} & \cdots & \lambda_{2N}\end{bmatrix}$, to then express the measurements as:

$$\mathcal{T} = [\boldsymbol{\lambda}; \dot{\mathbf{X}}, \dot{\mathbf{Y}}, \mathbf{D}] \tag{6.9}$$

which from Chapter 3, it is known that it corresponds with the Canonical Polyadic Decomposition (CPD). So, if we form a tensor $\mathcal{T}$ containing the transmission parameters of k lines of different length, but with identical excitation transitions, the CPD decomposition gets the matrices $\dot{\mathbf{X}}$, $\dot{\mathbf{Y}}$ and $\mathbf{D}$ in equations (6.7) and (6.8) except for a permutation matrix and a scaling factor matrix. Note that the CPD is a tensor decomposition that is unique, up to a permutation and scaling factors, when the sum of the factor matrices ranks, defined as the number of linearly independent columns, is greater or equal to $2F + 2$ being F the number of summing elements in (6.4). In the MMTRL procedure for N non-degenerated modes, matrices $\dot{\mathbf{X}}$, $\dot{\mathbf{Y}}$ and $\mathbf{D}$ are ranked $2N$ and the summing elements in (6.4) is $2N$. Therefore, uniqueness holds since $6N$ is greater than $4N + 2$ for any number of propagating modes.

In order to estimate the propagation constant, the first thing to be done after the CPD decomposition to get the matrix $\mathbf{D}$ which has the required information, is to get ride of the scaling factors affecting it. To do so, it necessary to realize that the permutation, as it has already been commented, does only affect to the columns of $\mathbf{D}$, not to its rows (see (6.8)). Therefore, lines in (6.8) are sorted according to the order in which the measured data are included in $\mathcal{T}$. Also, in the multimode case, we have two kinds of arbitrary scale factors that could affect $\mathbf{D}$: one of them multiplies the entire matrix, the other multiplies the columns with a positive propagation constant and divides the column with a negative one. The latter can be interpreted as a change of the reference plane for each mode because of the exponential form of the matrix terms. Therefore, some information about the line lengths should be used to fully determine the $\mathbf{D}$ matrix. To ensure that the best linear estimation of the propagation constants can be found, at least when only considering the zero-mean additive white Gaussian noise (AWGN), the Gauss-Markov formulation has been included. Hence, the obtainment of the propagation constant has been separated from the deduction of the scale factors. So, a two-step normalization has been established as in the monomode case. The procedure is very similar to the one in

Chapter 3 but it is repeated here because some precautions must be taken when dealing with multimode transmission sections. First, for simplicity, the length of the line chosen as thru is set as zero. Then, each of the columns in (6.8) is normalized by the value on the position of the thru. This normalization gives special precedence to the accuracy of the result for the line chosen as thru. But as it has been repeated along this thesis, the objective of the CPD is to make an approximation to the $\dot{\mathbf{X}}$, $\dot{\mathbf{Y}}$ and $\mathbf{D}$ values that best fit the tensor $\mathcal{T}$, without prioritizing any of the lines. This is why a second step must be followed. However, in this multimode case, several modes have to be identified to be able to do a fine-tuning of the scale factor affecting the exponentials. Therefore, the permutation is removed (explained later on) and then the second step based on an optimization is carried out. The optimization finds the ξ factor that best fits that all the elements in $\mathbf{e_i}$, multiplied by their corresponding elements in $\mathbf{e_{i+N-1}}$, are equal to one. So, this second step is the fine-tuning of a factor ξ that must divide both columns in (6.8). The optimization problem for k lines and N modes is stated as:

$$\xi = \min_{\nu} \sum_{j=1}^{N} \sum_{i=1}^{k} \left| \mathbf{e}_{i,j} \mathbf{e}_{i,N+j} - \nu^2 \right|^2 \tag{6.10}$$

where the summation includes the thru, and the sign of ξ is chosen so that the terms corresponding to the thru in the normalized $\mathbf{D}$ are close to $+1$ (and not to -1).

The permutation, that should have already been removed in order to properly apply (6.10), consists on comparing the modes propagation constant with their estimations taken from the simulation of the transmission medium. More precisely, the permutation $\mathbf{P}$ is found by minimizing the distance between the exponential terms of $\mathbf{D}$ and the exponentials calculated with the estimations of the modes propagation constant.

Then, the values of the propagation constants for each of the N modes are calculated at each frequency, as given by each of the elements in the columns of $\mathbf{D}$ (excluding those corresponding to the thru). The possible phase jumps are then removed (the phase is unwrapped) so that the resulting propagation constants are continuous with frequency. Also here, the propagation constants of the waves propagating in both directions are averaged to minimize the influence of second-

order errors that may arise from differences between the connectors. Hence, $k-1$ values of γ are obtained for each of the N propagating modes.

The $k-1$ propagation constants are then optimally combined for each of the modes using the equation presented in Chapter 3, which has been repeated here for convenience:

$$\hat{\gamma} = \frac{\mathbf{L}^H \mathbf{V}^{-1} \mathbf{G}}{\mathbf{L}^H \mathbf{V}^{-1} \mathbf{L}} \tag{6.11}$$

where the superindex H stands for hermitian transpose. And, $\mathbf{L}$, size $(k-1)\times 1$, is the array containing all the Δl_{ij} values, $\mathbf{G}$ of size $(k-1)\times 1$ is the array with the $k-1$ values of γ_i. And $\mathbf{V}$ of size $(k-1)\times(k-1)$ is the measurement of the noise covariance that can be calculated assuming that there is no correlation between the measurement of the different lines and that they are all equally noisy:

$$\mathbf{V}^{-1} = \frac{1}{\sigma_i^2} \begin{bmatrix} 1-\frac{1}{k} & -\frac{1}{k} \\ -\frac{1}{k} & 1-\frac{1}{k} \end{bmatrix} \tag{6.12}$$

where σ_i is the variance of the noise in the individual line measurements, not being necessary its determination because of its appearance in the numerator as well as in the denominator of (6.11).

6.3 Estimation of Propagation Constants Using the Multimode Multiline TRL Algorithm

In order to evaluate the validity of the MMTRL algorithm to estimate the propagation constant for several modes at the same time, a WR-90 waveguide has been measured in a band in which modes with a cut-off frequency above the TE_{30}'s cannot propagate. To do so, the TE_{10}/TE_{30} mode launcher designed in the previous chapter has been used for the excitation of these two modes into a WR-90. Therefore, the measurable band has been defined from 20.5 to 23.5 GHz. However, since measuring waveguide losses is very tricky because of the instrumental noise, it has been decided to fill the waveguide with a dielectric to ensure that the measured losses are above the noise level. FOREX ($\epsilon_r = 1.7$ and $\tan\delta = 0.0035$) has been chosen as the dielectric since it permits the measurement of the propagation constant of both modes, the TE_{10} and the TE_{30}, in the mentioned band. Note that

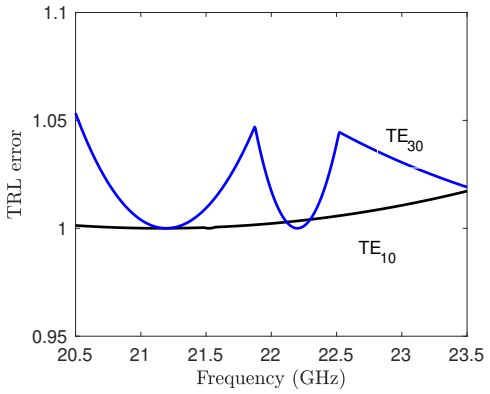

Figure 6.1: MMTRL error for the multimode propagation of the TE_{10} and TE_{30} in a WR-90 filled with FOREX.

the symmetry of the problem's geometry (launcher and waveguide) does not permit the excitation of the TE_{m0} with m even. And, that the permittivity constant has a value which does not let any TE_{m0} mode with m odd above the TE_{30} to propagate.

The estimation of the propagation constant by means of the MMTRL algorithm requires the measurement of several waveguide sections that do only differ in length. The choice of the sections' length should make their electric frequency response as much different as possible in order to diminish the numerical uncertainties of the procedure, as it is the case in the monomode algorithm. In short, for the multimode propagation, length differences between sections should differ from $\lambda/2$ as much as possible for all the involved modes. So, these differences have been increased simultaneously for both modes (TE_{10} and TE_{30}) by means of an optimization program. The mode with the shortest wavelength will always present more uncertainty for a set of sections, which reinforce the usefulness of the multiline approach compared to other methods. It has been arbitrary stated that the estimation will be carried out with four sections. Fig. 6.1 shows for both modes the minimum TRL error, calculated as the minimum error for each of the possible pairs, after the optimization process. The optimal length differences between sections are given in Table 6.1.

Table 6.1: Optimal length differences between sections.

Δ lengths (mm)	0	2.8	11.6	24.74

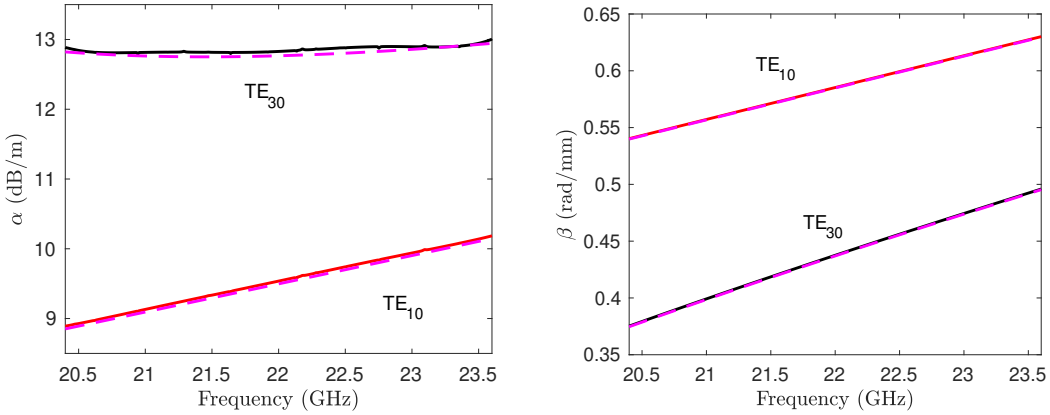

(a) **(b)**

Figure 6.2: Simulated frequency response of the TE_{10} and TE_{30} propagation constants in WR-90 filled with FOREX. Discontinuous lines: Analytic results. Continuous lines: MMTRL estimation.

6.3.1 Simulation Results for the Propagation Constant Estimation for Several Modes Simultaneously

First of all, the algorithm has been checked by simulation. The waveguide sections have been defined making use of the analytical expressions. The TE_{10}/TE_{30} mode launcher has been simulated with HFSS. Then, the waveguide sections have been connected to the launchers by means of the circuital tools of ADS. It is important to highlight that in order to avoid mesh asymmetries only half of the structures have been simulated. The estimation of the real and imaginary parts of the propagation constants are shown in Fig. 6.2. Discontinuous traces are the analytical propagation of both modes for a WR-90 waveguide filled with forex and continuous lines are the result of the estimation of the propagation constant by means of the MMTRL procedure. In conclusion, both propagation constants have been perfectly estimated, and therefore, the MMTRL is proved to be useful in the determination of propagation constants with high accuracy (the accuracy can be improved by the simple task of adding more sections to the set of measurements).

6.4 Implementation of the MMTRL calibration

The non-idealities of the vector network analyzer are collected, as shown in (6.3), into two wave-chain matrices: $\mathbf{X}$ for port 1 and $\mathbf{Y}$ for port 2. Note that the measurement of a multimode device can be expressed like in (6.3) but substituting the matrix $\mathbf{T}^i$ by the Device Under Test (DUT) wave-chain matrix, $\mathbf{T}_{DUT}$. Therefore, a multimode multilinear calibration can be carried out by means of the CPD if the $\mathbf{X}$ and $\mathbf{Y}$ are known. The measured wave-chain matrix is:

$$\mathbf{M}_{DUT} = \mathbf{X}\mathbf{T}_{DUT}\mathbf{Y} \tag{6.13}$$

The CPD gives the $\mathbf{X}$ and $\mathbf{Y}$ but scaled and permuted. Therefore, a processing must be made to get them. First of all, the $\dot{\mathbf{X}}$ and $\dot{\mathbf{Y}}$ matrices in (6.7) are made consistent with a VNA measurement. To do it, the permutation found for $\mathbf{D}$ and the scaling factors mentioned in Section 6.2 are conveniently applied to these matrices, so $\mathbf{X}$ and $\mathbf{Y}$ are found. However, it could exist a diagonal matrix, $\mathbf{K}$, multiplying $\mathbf{X}$ and $\mathbf{Y}$ containing scaling factors affecting both matrices but not $\mathbf{D}$. Let us then express $\mathbf{X}$ as:

$$\mathbf{X} = \mathbf{X_0}\mathbf{K} = \mathbf{X_0}\mathbf{K_0}\alpha \tag{6.14}$$

Note that the diagonal matrix $\mathbf{K}$ has been expressed as $\mathbf{K_0}\alpha$, being α an unknown scalar.

From the measurement of the thru:

$$\mathbf{M} = \mathbf{X}\mathbf{I}\mathbf{Y} \tag{6.15}$$

where I is the identity matrix (response of the thru).

If (6.15) is solved for $\mathbf{Y}$ we get that:

$$\mathbf{Y}^{-1} = \mathbf{M}^{-1}\mathbf{X} = \mathbf{M}^{-1}\mathbf{X_0}\mathbf{K} = \mathbf{Y_0}\mathbf{K} = \mathbf{Y_0}\mathbf{K_0}\alpha \tag{6.16}$$

So, to get the matrix of the DUT, the next equation must be executed:

$$\begin{aligned}\mathbf{T}_{DUT} =& \mathbf{K}^{-1}{\mathbf{X_0}}^{-1}\mathbf{M}_{DUT}\mathbf{Y_0}\mathbf{K} \\ =& {\mathbf{K_0}}^{-1}{\mathbf{X_0}}^{-1}\mathbf{M}_{DUT}\mathbf{Y_0}\mathbf{K_0}\end{aligned} \tag{6.17}$$

Note that it is not necessary to find α since the objective is not to get $\mathbf{X}$ and $\mathbf{Y}$ but the DUTs response. So, also in the MMTRL calibration there is a one-dimensional ambiguity that it is not solved.

In order to get the matrix $\mathbf{K_0}$ the steps in [1] must be followed, and they will not be repeated here. It will only be commented that the measurement of a reflective standard which presents interaction between all the considered modes (and only between them) must be carried out to be able to solve the procedure's equations.

Summarizing, the correction coefficients are found following the same steps as in [1], that is, making use of the measurements of the multimode reflect at both ports of the VNA.

6.5 Simulated Results for the MMTRL calibration

Along this section, the simulation of the MMTRL calibration in the multimode band that goes from 20.5 to 23.5 GHz has been carried out for the TE_{10} and TE_{30} modes. To do it, the TE_{10}/TE_{30} mode launcher designed in the previous chapter has been used to generate both modes in WR-90 sections. It has been simulated with HFSS using the $H-$plane symmetry to avoid the excitation of other modes because of mesh asymmetries. Therefore, the WR-90 sections and the DUTs (some filters) have also been simulated with this symmetry. In this case, all the simulations of the devices have been carried out with HFSS. Then, the devices have been connected with the circuital tool of ADS and the results processed with Matlab. The WR-90 sections have been exactly the same than for the estimation of the propagation constant of the WR-90 waveguide filled with FOREX given in Table 6.1. Obviously, these lengths are not optimal when the waveguides are empty. However, being the accuracy for the characterization of filters in a multimode band less demanding than the propagation constant estimation, it has been decided to keep them to avoid the manufacturing process of more WR-90 sections.

To complete the calibration, the design of a multimode reflect has been carried out. Basically, it is a symmetric width variation. This design permits to have an interaction between the TE_{10} and TE_{30} modes, which is required in order to perform the calibration. Fig. 6.3 shows the 3D model of the multimode reflect and

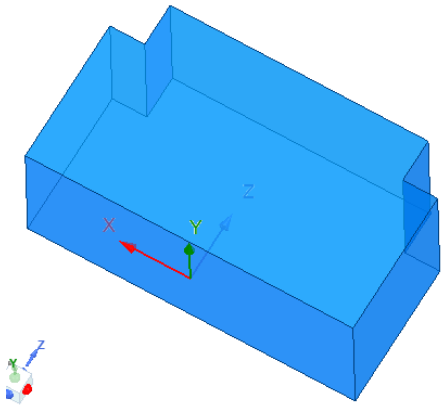

Figure 6.3: 3D model of the TE_{10}/TE_{30} reflect.

Fig. 6.4 its frequency response, in which port 1 refers to the TE_{10} and port 2 to the TE_{30} mode.

The calibration has been carried out connecting directly the reflect to the launcher, which means that it has not been placed at the calibration reference plane (center of the thru). Therefore, all measurements must be shifted, making use of the estimation of the propagation constant, in order to be able to get the phases response properly. Also, not to mislead the reference plane, special attention must be payed when using the information for the phase of the reflect.

6.5.1 Results for the Bandpass Filter

The $H-$plane bandpass filter designed in the previous chapter has been used to prove through simulations the validity of the MMTRL calibration. To do so, half of the filter has been simulated with HFSS, which avoids mesh asymmetries that could generate TE_{m0} modes with m even. The 3D model of the filter together with the electrical ports nomenclature has been repeated for convenience in Fig. 6.5. To simulate the VNA measurement procedure, the TE_{10}/TE_{30} launchers have been connected using ADS to the filter. The resulting scattering matrix has been processed with Matlab. Fig. 6.6 shows the results. The ideal response of the filter refers to the results that HFSS gives when the filter is simulated. On the other hand, the MMTRL filter response refers to the filter's frequency response extracted

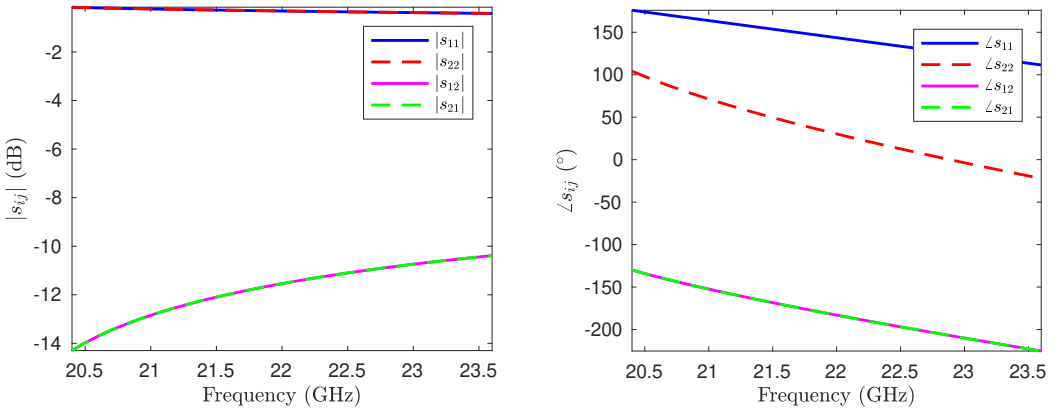

(a) **(b)**

Figure 6.4: HFSS frequency response of the TE_{10}/TE_{30} multimode reflect in Fig. 6.3.

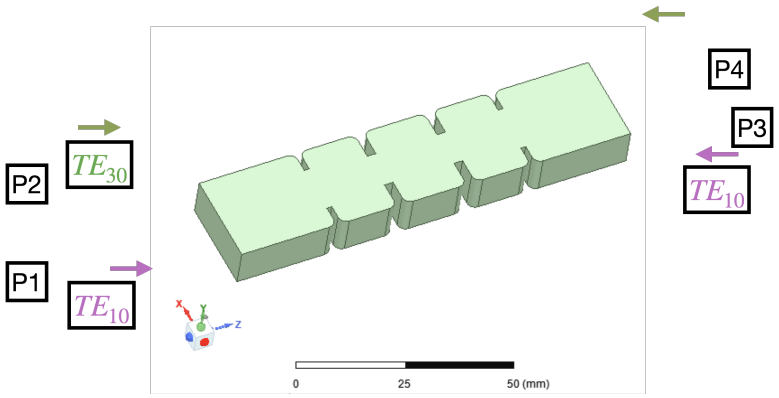

Figure 6.5: Ports definition in the 3D model for the $H-$Plane WR-90 Chebyshev bandpass filter.

from the MMTRL procedure (the filter is not measured alone, but through the excitation of the TE_{10}/TE_{30} launcher). Both responses are equal (not distinguishable in Fig. 6.5), and so, it can be said that the MMTRL has well recovered the filter's frequency response in modulus and phase.

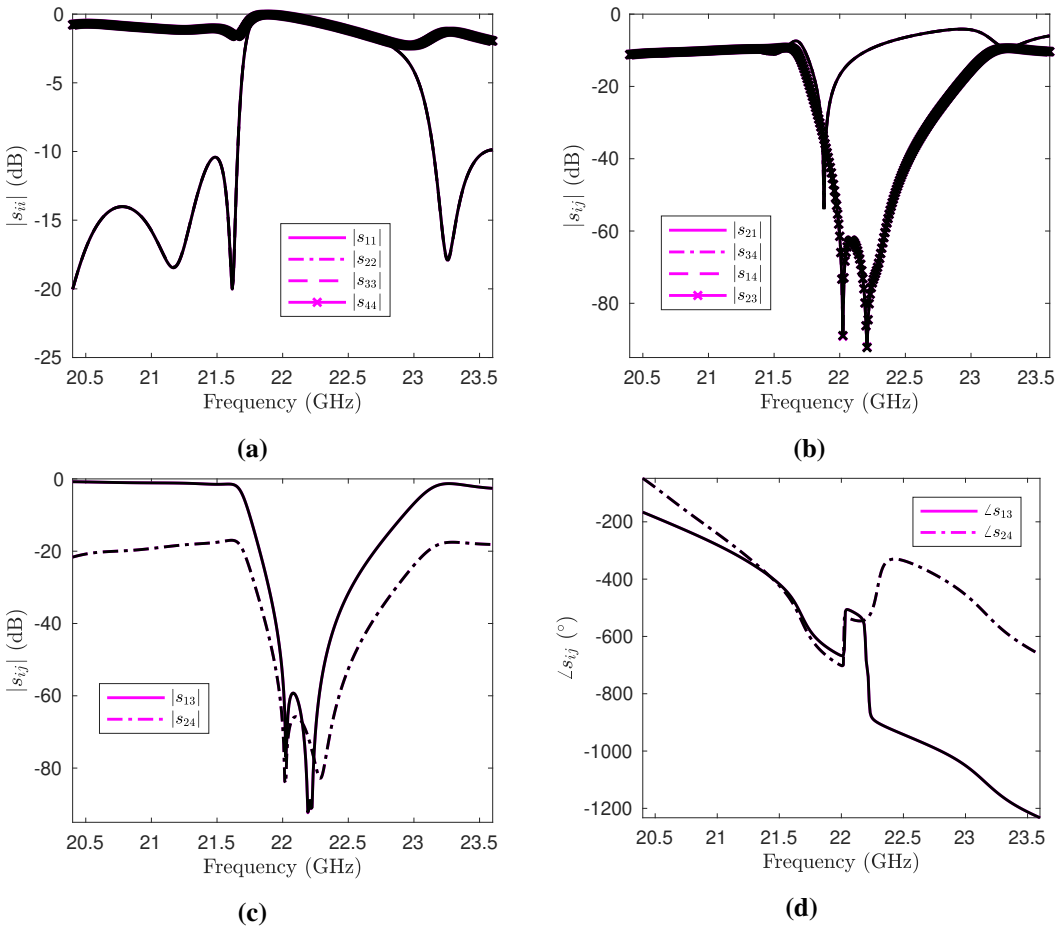

Figure 6.6: $H-$Plane WR-90 full-wave frequency response of the Chebyshev band-pass filter in the multimode band. Black: HFSS filter ideal response. Magenta: MMTRL filter response.

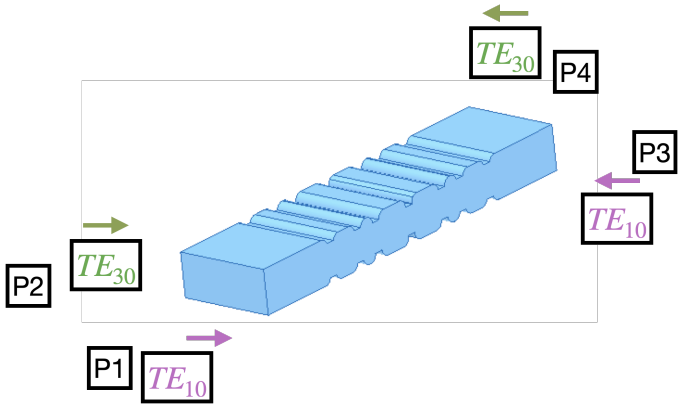

Figure 6.7: Ports definition in the 3D model of the $E-$Plane WR-90 Zolotarev low-pass filter.

6.5.2 Results for the Low-pass Filter

To verify the proper functioning of the MMTRL calibration algorithm, also, the $E-$plane low-pass filter designed in the previous chapter has been used through simulations. As in the previous device, to avoid asymmetries in the mesh, and therefore, the excitation of undesired modes, only half of the filter has been simulated with HFSS. The 3D model of the filter together with the electrical ports nomenclature has been repeated for convenience in Fig. 6.7. Using the circuit tool of ADS, the filter has been connected to the TE_{10}/TE_{30} launchers to simulate the VNA measurement procedure. The resulting scattering matrix has been processed with Matlab and Fig. 6.8 shows the results. The ideal response of the filter refers to the results that HFSS gives when the filter is simulated. On the other hand, the MMTRL filter response refers to the filter's frequency response extracted from the MMTRL procedure (the filter is not measured alone, but through the excitation of the TE_{10}/TE_{30} launcher). Also, in the calibration of the low-pass filter, we get that both responses are equal (not distinguishable in Fig. 6.8), which permits to conclude that the MMTRL calibration permits to accurately characterize multimode devices in modulus and phase.

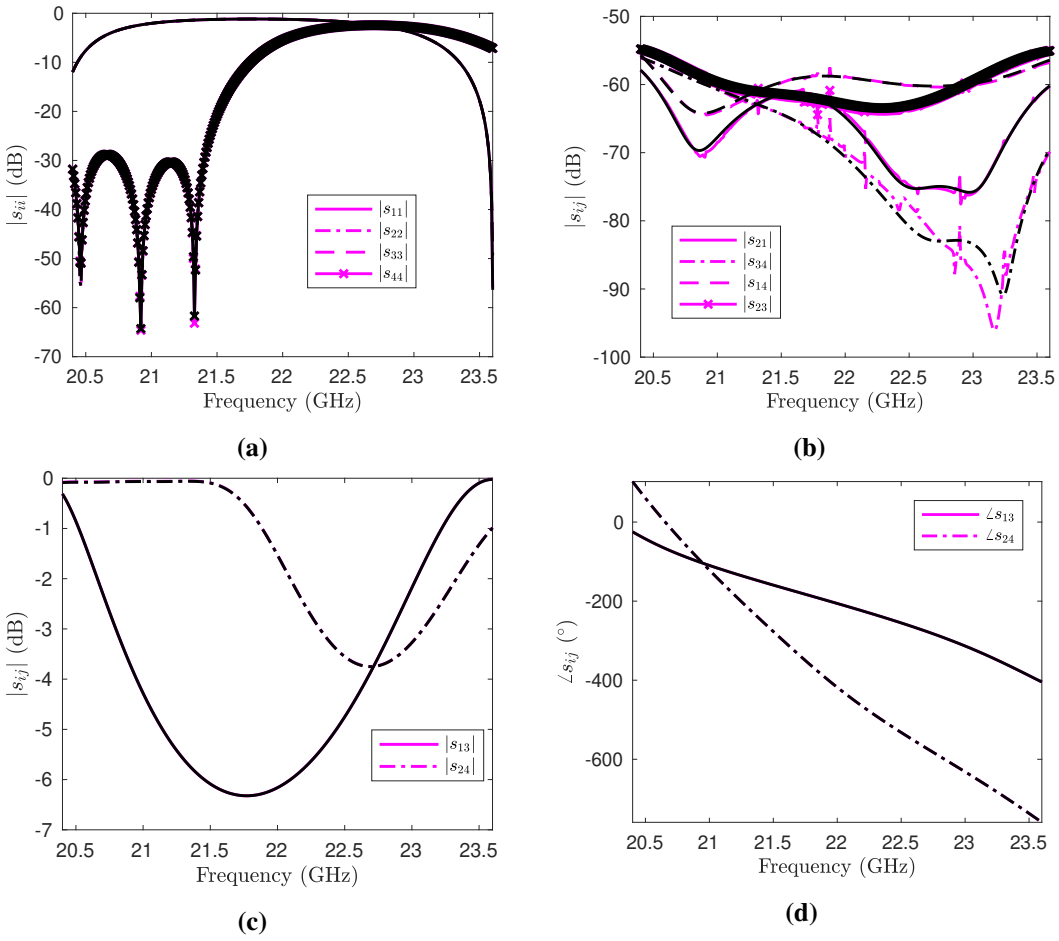

Figure 6.8: $E-$Plane WR-90 full-wave frequency response of the Zolotarev low-pass filter in the multimode band. Black: HFSS filter ideal response. Magenta: MMTRL filter response.

6.6 Measured Results for the MMTRL calibration

To verify by experiment the MMTRL calibration, two bandpass filters have been measured. An important remark is that both of them do only generate and permit the propagation of the TE_{10} and TE_{30} from 20.5 to 23.5 GHz and their physical interface is WR-90, so they can be excited by the mode launchers designed in Chapter 5. These filters have been designed at ESA and at UPM years ago, therefore, in order to get their monomode frequency response, their physical dimensions have been measured with a caliper and they have been reproduced with HFSS. This procedure permits to get their theoretic response with conventional full-wave software packages in both bands, the monomode and the multimode.

6.6.1 Monomode Response of the Bandpass Filters

Two bandpass filters have been measured, using a conventional monomode WR-90 TRL calibration. Fig. 6.9 shows a photography of the measurement for the "width variation" $H-$plane filter in its monomode band and the results. It has also been included the HFSS simulation response, showing a good agreement between simulation and measurement.

The second filter that has been measured is a sheet filter (mainly known as all-metal insert E-plane filters). The photography of the measurement and the results are shown in Fig. 6.10, including, also in this case, the scattering parameters derived by HFSS. Note, that the simulated response is shifted toward higher frequencies compared to the measurement (Fig. 6.10b).

6.6.2 Multimode Response of the Bandpass Filters

Both filters, Fig. 6.9a and Fig. 6.10a, have been measured in the multimode band, from 20.5 to 23.5 GHz, making use of the MMTRL calibration. The modes to be measured were the TE_{10} and the TE_{30}. In order to do it properly, several standards had to be measured, in this case: four WR-90 sections, a reflect which generates interaction between the measured modes and the filters.

The manufacturing of the WR-90 waveguide sections has been challenging since it was mandatory to manufacture them in one piece. In order to do it, a long

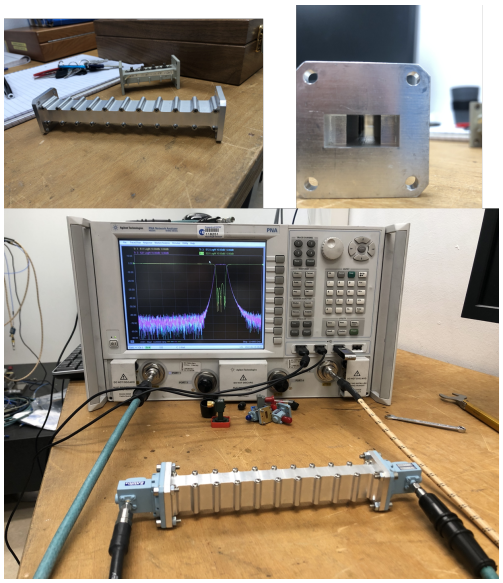

(a)

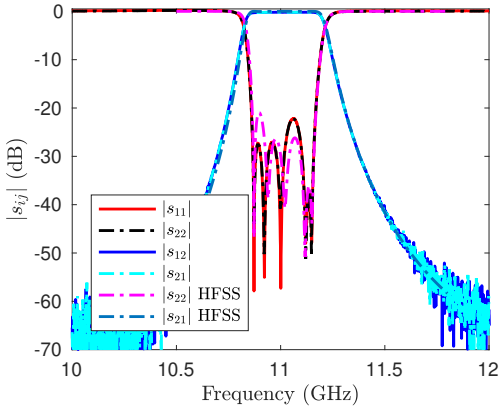

(b)

Figure 6.9: Width variation WR-90 bandpass filter ($H-$plane filter).

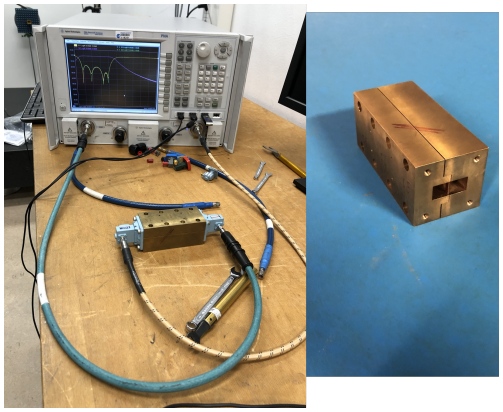

(a)

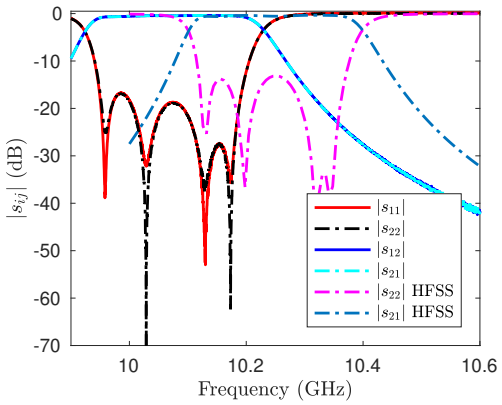

(b)

Figure 6.10: Sheet WR-90 bandpass filter (all-metal insert E-plane filters).

Table 6.2: Manufactured length differences between sections.

lengths (cm)	9.960	10.236	11.116	12.478
Δ lengths (mm)	0	2.760	11.560	25.180

section of WR-90 that was available in our facilities, has been cut to form the four waveguides with the lengths defined in Table 6.1. Afterwards, flanges have been welded. In this last manufacturing process, some piece-blending happened, and hence, the final dimensions of the sections have been modified a little bit. Table 6.2 shows the final lengths, and the difference between sections taking the shortest as reference.

Fig. 6.11 shows photographies of all the standards and some of the measurements, which were carried out at ESTEC. It must be mentioned that because one of the filters was not properly manufactured for this set up, the MMTRL calibration process was repeated at Universidad Carlos III, once the connection problem was solved. On the other hand, Fig. 6.11d shows that a four-port VNA has been preferred. The motivation came from the reduction of the number of connections and disconnections of the launchers since their frequency response must remain the same from measurement to measurement. Finally, the reflect has been measured directly connected to the WR-90 port of the launchers, which obliges to take into account the phase shift introduced by half of the shorter WR-90 section (taken as reference plane in the procedure described above).

The multimode measurement results for the "width variation" filter are given in Figs. 6.12 and 6.13. It has also been included in those figures the electric port nomenclature. Furthermore, the HFSS simulated response has been depicted together with the measured scattering parameters for comparison. Both responses, simulated and measured, agree very well even for the phase response. It can then be concluded that the MMTRL calibration process is an accurate method to calibrate several modes simultaneously.

Finally, the sheet filter has also been measured in the multimode band and some of the most representative results are shown in Fig. 6.14 with the electric port nomenclature depicted in Fig. 6.14a. In this case, the HFSS simulated response is

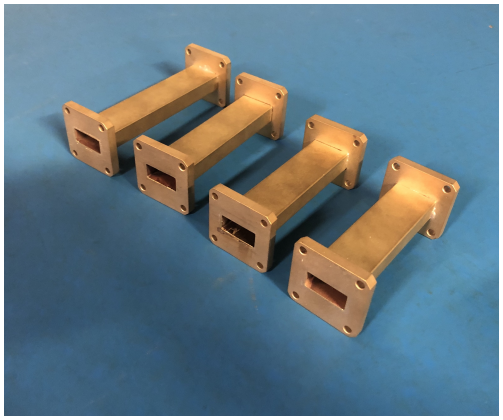

(a)

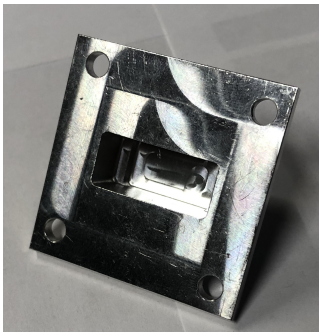

(b)

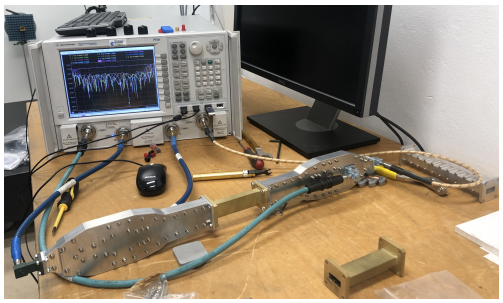

(c)

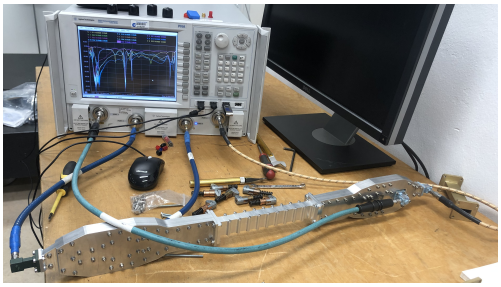

(d)

Figure 6.11: Photographies of the MMTRL calibration standards and photographies of some measurements carried out at ESTEC and at Universidad Carlos III. a) Photography of the WR-90 sections used in the calibration process. b) Photography of the manufactured multimode reflect. c) Photography of the measurement of a waveguide section. c) Photography of the measurement of a filter.

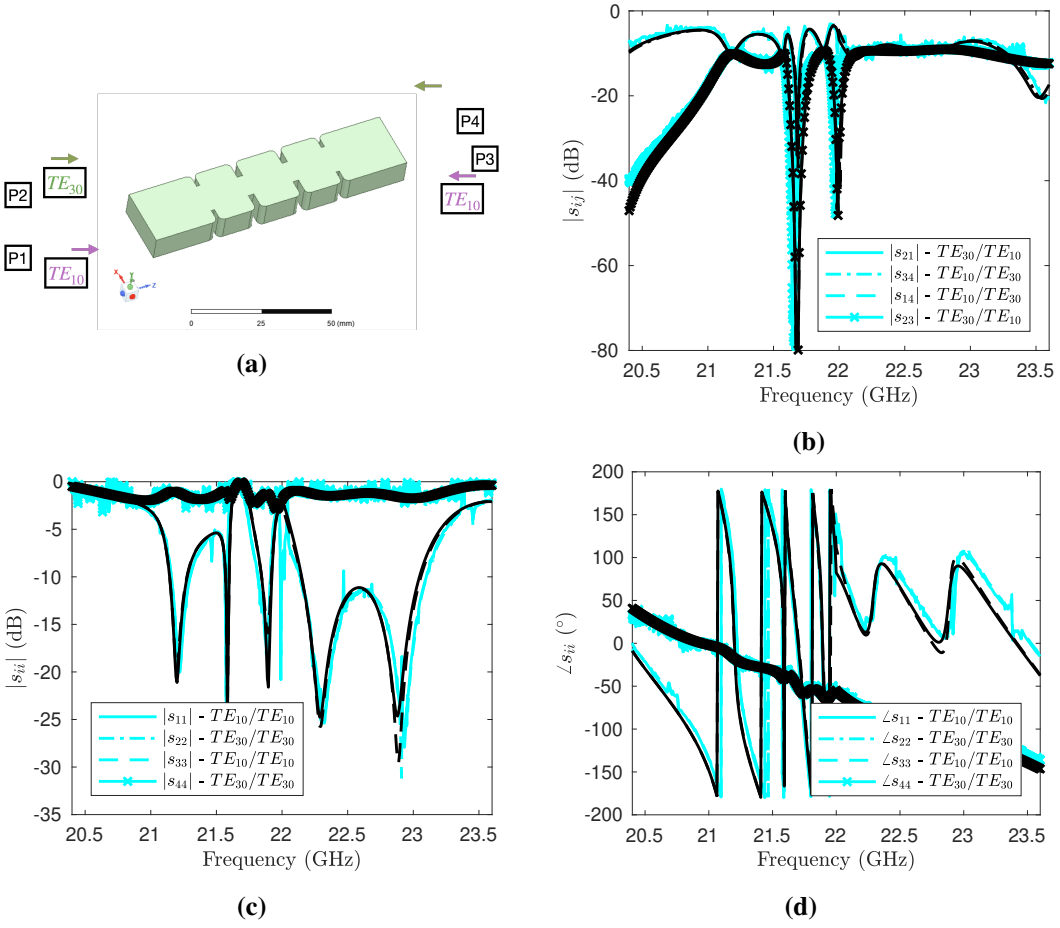

Figure 6.12: Frequency response of the TE_{10} and TE_{30} of the width variation WR-90 bandpass filter ($H-$plane filter) in a multimode band. Black: HFSS simulation response. Cyan: Measurements.

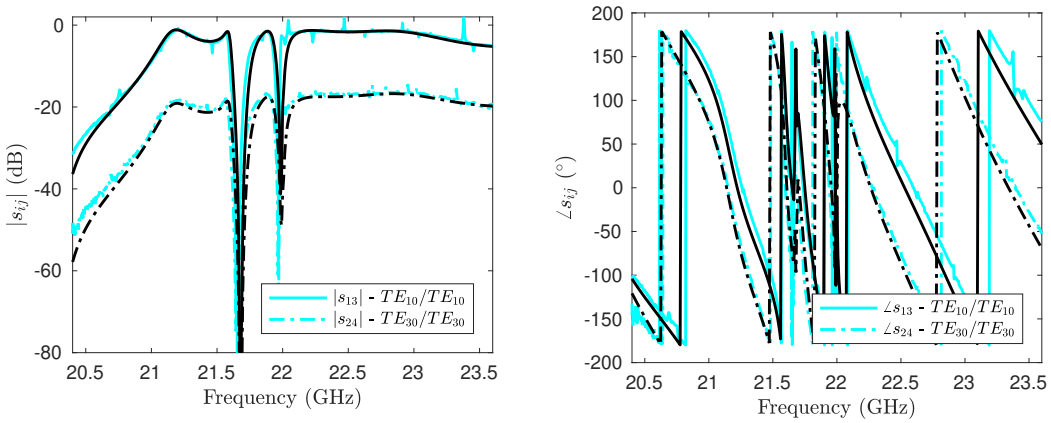

(a) **(b)**

Figure 6.13: Frequency response of the TE_{10} and TE_{30} of the width variation WR-90 bandpass filter ($H-$plane filter) in a multimode band. Black: HFSS simulation response. Cyan: Measurements.

shifted toward higher frequencies as it was the case in the monomode band, which seems to confirm that the MMTRL calibration process works properly.

6.7 Conclusions

In this chapter, multimode band measurements focusing on propagation constant measurements and calibration have been discussed, and then new methods have been developed. The main advantage of the presented work is that all modes can be accurately taken into account. It is worth mentioning that higher order modes will always present a little more uncertainty in their calibrated responses compared to the fundamental mode. However, the uncertainty can be diminished by adding more and more transmission medium sections to the standards of the calibration. The measurements carried out here, have been made with only four sections (including the thru) and results are satisfactory. Both the module and phase of two WR-90 bandpass filters have been perfectly characterized in a multimode band for the TE_{10} and the TE_{30}. It must be highlighted that the novel multiline multimode TRL calibration developed in this work permits to get high accuracy in all measured modes for a broadband measurement, which was not possible with previous methods.

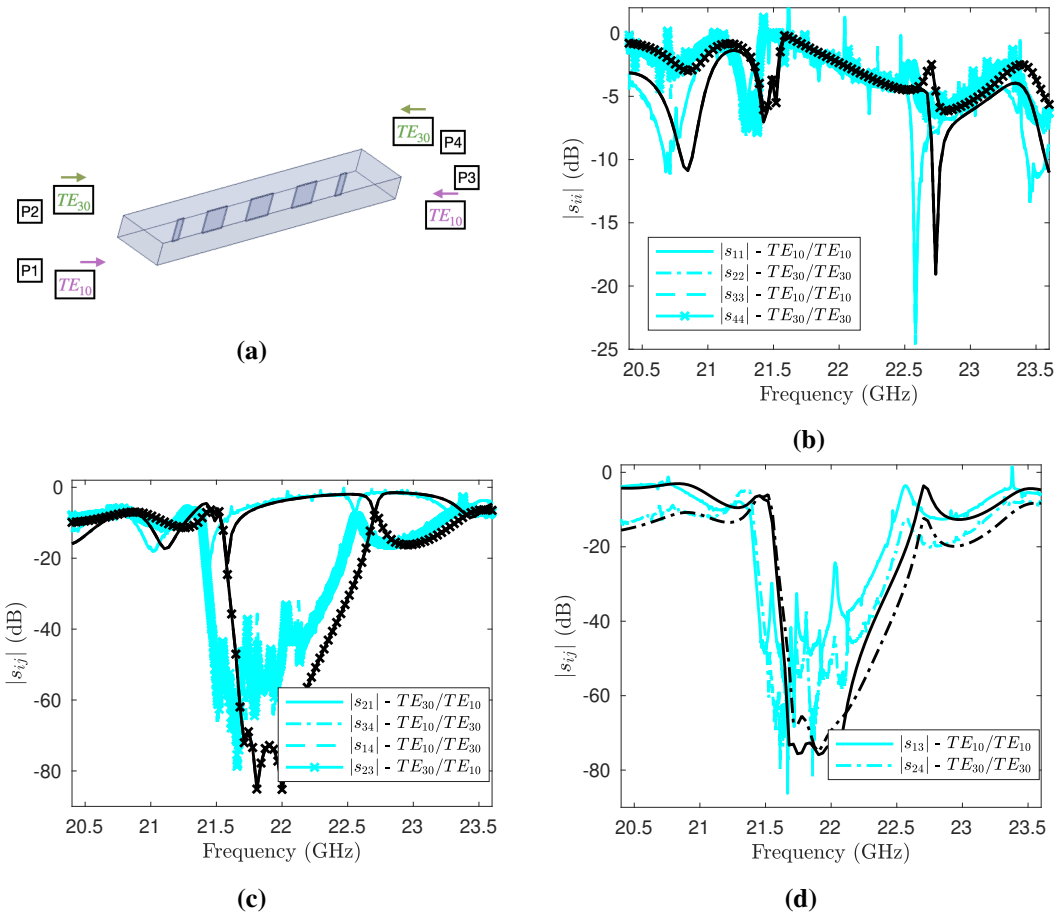

Figure 6.14: Frequency response of the TE_{10} and TE_{30} of the sheet WR-90 bandpass filter in a multimode band. Black: HFSS simulation response. Cyan: Measurements.

References

[1] C. Seguinot, P. Kennis, J.-F. Legier, F. Huret, E. Paleczny, and L. Hayden, "Multimode trl. a new concept in microwave measurements: theory and experimental verification," *IEEE Transactions on Microwave Theory and Techniques*, vol. 46, no. 5, pp. 536–542, 1998. 177, 188

[2] M. Wojnowski, V. Issakov, G. Sommer, and R. Weigel, "Multimode trl calibration technique for characterization of differential devices," *IEEE Transactions on Microwave Theory and Techniques*, vol. 60, no. 7, pp. 2220–2247, 2012. 177

[3] T. Buber, A. Rodriguez, L. Dunleavy, N. Kinayman, A. Jenkins, I. Gresham, A. Khalil, and R. Wohlert, "Improved multimode calibration standards for 40 ghz measurements of active devices," in *65th ARFTG Conference Digest, 2005. Spring 2005*, 2005, pp. 5 pp.–. 177

[4] H.-C. Lu and T.-H. Chu, "Antenna polarimetric calibration using multi-mode trl calibration method and its extension," in *APMC 2001. 2001 Asia-Pacific Microwave Conference (Cat. No.01TH8577)*, vol. 3, 2001, pp. 1315–1317 vol.3. 177

[5] A. Morini, M. Guglielmi, and M. Farina, "A technique for the measurement of the generalized scattering matrix of overmoded waveguide devices," *IEEE Transactions on Microwave Theory and Techniques*, vol. 61, no. 7, pp. 2705–2714, 2013. 177

CHAPTER

7

Design of Cross Sections for Monomode Low-Loss Transmission Media

7.1 Introduction

There are several waveguides that are commonly used in microwave systems as the ones with circular and rectangular cross section shapes. However, it seems that they have been chosen because of their simplicity in terms of the control of their cut-off frequencies or their manufacturing easiness. Nowadays, full-wave commercial programs like HFSS or CST permit to analyze in reasonable time and enough accuracy the electric characteristics of any cross section shape waveguide. On the other hand, manufacturing processes are experimenting a huge change since new processes like 3D printing have emerged in the microwave industry. Therefore, nowadays it is posible to think that a transmission medium better in propagation constant (losses and bandwidth) could exist compared to the conventional ones. So, this is the main objective of this chapter, to analyze the propagation characteristics of known transmission media and then to look for their improvement through the optimization of their attenuation constant in a pre-defined bandwidth. It must

be highlighted that along this chapter only monomode transmission media are going to be considered. The organization of this chapter is as follows. First of all, the analysis of conventional waveguides is going to be done in Section 7.2 once a comparison procedure has been stated. Then, the best smooth walled transmission media are made periodic in Section 7.3 and their characteristics are compared to the smooth walled case. Also in Section 7.3 the analysis and optimization of gap waveguides are included since they can be considered periodic transmission media and they are nowadays very popular in the technical literature. Besides, some authors have associated them with low-loss propagation [1, 2]. Finally, in Section 7.4 some conclusions are given.

7.2 Smooth Walls

In this section different smooth walled monomode waveguides are analyzed in terms of their propagation constant and the monomode bandwidth they offer. First of all, a comparison criteria has been developed, and then, several shapes have been compared: circular, elliptical, rectangular, "potato", "cigar" and groove waveguides. All the considered transmission media have been closed to make them useful for space applications.

7.2.1 Comparison Criteria

Along this section a transmission media comparison criterium has been stated. The main idea of the comparison is to be able to take easily into account losses and bandwidth at the same time when defining an optimization cost function. Criteria have been defined making use of the rectangular waveguide characteristics. Three comparison criteria have been considered:

1. fixing the bandwidth $f_{c1} - f_{c0}$;
2. fixing the fundamental mode cut-off frequency, f_{c0}, and see what is the bandwidth it gives before the first higher order mode starts propagating, f_{c1};
3. fixing the frequency at which the first higher order mode starts propagating, f_{c1}, and see what is the bandwidth the fundamental mode has $f_{c1} - f_{c0}$.

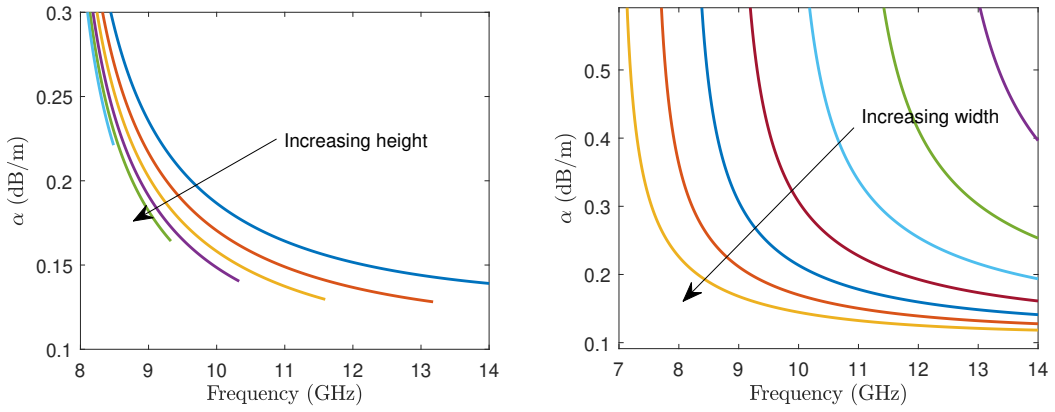

Figure 7.1: Losses and bandwidth characteristics for the rectangular cross section waveguide. Comparison criteria: a) fixing f_{c0} criterium 2; b) fixing f_{c1} criterium 3.

Criterium 1 has immediately been discarded for the purpose of this thesis, since it does not give any flexibility to modify the cross section in an optimization process. Criteria 2 and 3 might seem very similar. The results for both of them using the rectangular waveguide characteristics are shown in Fig. 7.1. The response of each waveguide has only been plotted for the monomode band. In Fig. 7.1a , the width of rectangular waveguides has been used to fix the fundamental cut-off frequency and a height variation has been carried out. On the other hand, in Fig. 7.1b, the height of the rectangular waveguide has been used to fix the first higher order mode cut-off frequency and then a width variation has been carried out. Both criteria permit to ask for a minimum bandwidth without stating a maximum one. In addition to that, at least a cut-off frequency must be fixed in order to avoid solutions which do only reduce the ohmic losses by decreasing the frequency. For optimization purposes, criteria 3 gives the most visible graph as the reader can deduce from Fig. 7.1. Furthermore, losses use to be lower nearer the appearance of the higher order mode, which makes criterium 3 more useful than criterium 2. Therefore, criterium 3 will be the one used along this thesis to compare different transmission media.

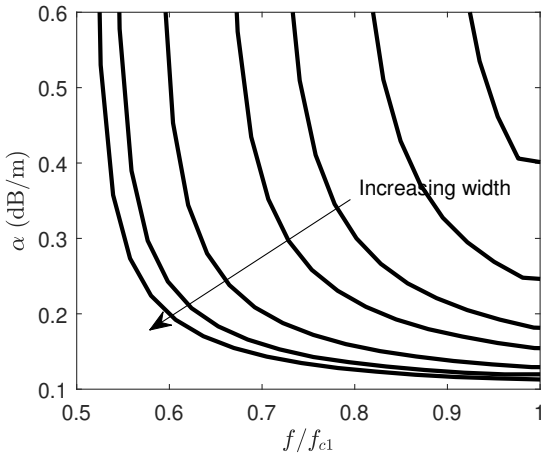

Figure 7.2: Attenuation constant for the rectangular waveguide.

7.2.2 Rectangular Waveguide

Fig. 7.1b shows that the best rectangular waveguide, for a fixed first higher order mode, is, as it is well known, the one with the biggest cross section surface, which means the one that makes the first and second higher order modes to be degenerated. In Fig. 7.2 the cut-off frequency of the higher order mode has been normalized, since the difference in losses between cross sections is independent of the frequency (this is not the case for its absolute value). However, structures are full-wave simulated with a cut-off of 14 GHz otherwise the comparison between different cross sections will be influenced by the conductor losses dependence on frequency.

7.2.3 Circular Waveguide

The circular waveguide is usually associated with low-loss because of its resonators characteristics in the filters design domain. However, as transmission medium, this cross section does only have a degree of freedom, the radius, which is used to fix the higher order mode cut-off frequency. Fig. 7.3 shows the attenuation constant as a function of frequency for the circular waveguide cross section.

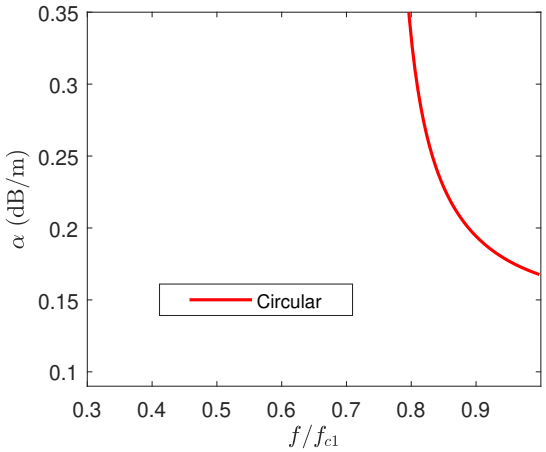

Figure 7.3: Attenuation constant for the circular waveguide.

7.2.4 Elliptical Waveguide

The elliptical waveguide has been for a long time under study because of its low-loss characteristics [3]. Besides, its modes are analytical, which in the past has been a big advantage compared to other topologies. However, manufacturing elliptical waveguides with classical procedures is difficult and so, expensive. Nowadays, with 3D printing it is a geometry that should be reviewed as a low-loss medium. Fig. 7.4 shows the attenuation constant as a function of frequency for the elliptical waveguide cross section. Once again minimum losses are achieved for the biggest surface.

7.2.5 Groove Waveguides

Groove waveguides have been developed as a low-loss medium. However, it was first analyzed as an open medium, similar to a parallel plate medium but with a protuberance in the center of the medium to confine the electromagnetic field. If the propagation constant is calculated for such a medium, very small losses are obtained [4]. Nonetheless, losses increase above the rectangular's when walls are considered. Along this thesis only closed media are considered because they are more practical thanks to their interference avoidance capability. Different geometries have been analyzed being the best ones in terms of losses represented in

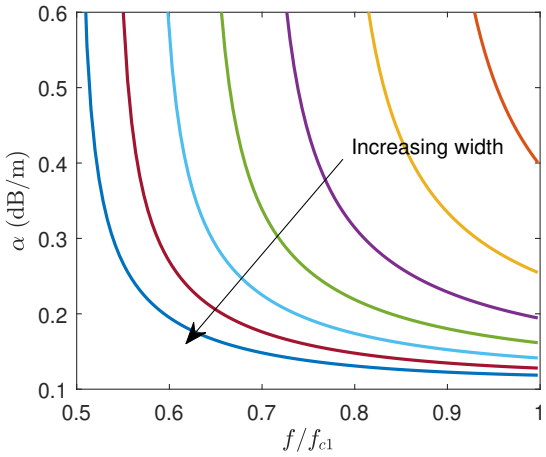

Figure 7.4: Attenuation constant for the elliptical waveguide.

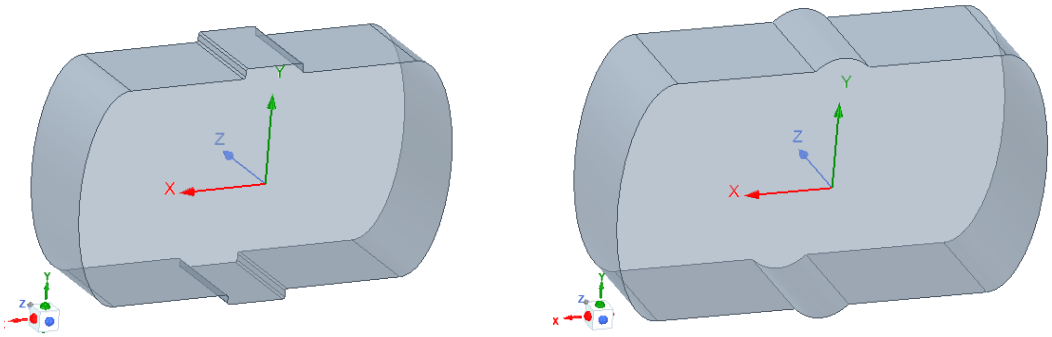

(a) **(b)**

Figure 7.5: 3D model for the analyzed groove waveguides: a) type 1; b) type 2.

Fig. 7.5. Note that in both cases, the parallel plates are closed with and elliptical cross section. Fig. 7.6 shows the attenuation constant as a function of frequency for the closed-groove waveguide cross section. For each of them, minimum losses are achieved when the surface is the biggest.

7.2.6 Cigar Waveguides

The cigar waveguide has been derived from the simplification of the optimal -in terms of losses- smooth waveguide, the so called “potato” that will be studied in the next subsection [5]. However, this cross section has its importance because

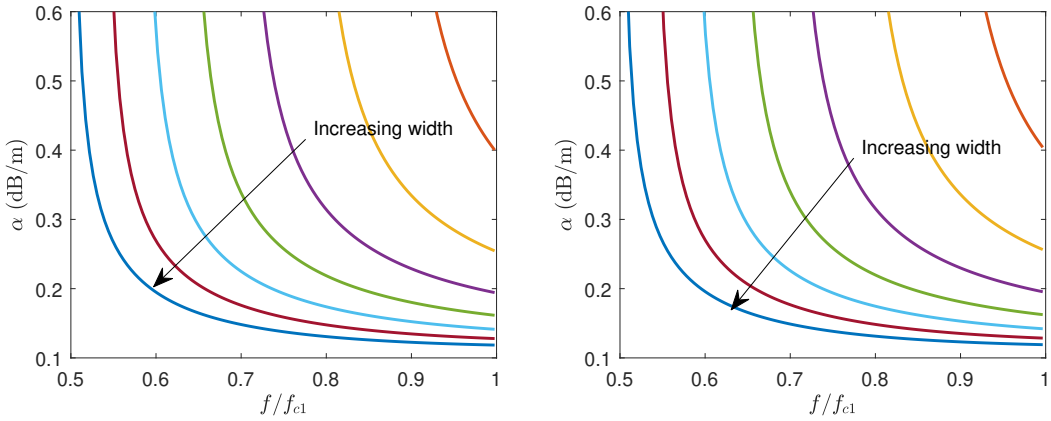

Figure 7.6: Attenuation constant for the groove waveguide: a) type 1; b) type 2.

of its easiness to be manufactured and because it has been the main solution for the low-loss problem in several projects [6]. However, it has lately been used as multimode medium. Usually, the cigar is defined as a parallel plate medium in which two circles are used to close it. Along this thesis, this cigar will be referred as "original cigar", and when ellipses are used to close the medium, the cross section will simply be referred as "cigar" or sometimes "elliptic cigar" . Fig. 7.7 shows the attenuation constant as a function of frequency for the closed-groove waveguide cross section. Once again minimum losses are achieved for the biggest surface.

7.2.7 Potato Waveguide

The potato waveguide, see Fig. 7.8, has been firstly presented by Suzuki and Hosono [5]. This cross section is the result of an optimization in terms of losses, without taking into account the bandwidth. However, the bandwidth is not practically reduced compared to a rectangular waveguide. The big inconvenience that the potato shape presents is that its manufacturing process is very complicated. That is why the original cigar waveguide has been presented as final result in [5]. Fig. 7.9 shows the attenuation constant as a function of frequency for the potato waveguide, only the optimum result is shown.

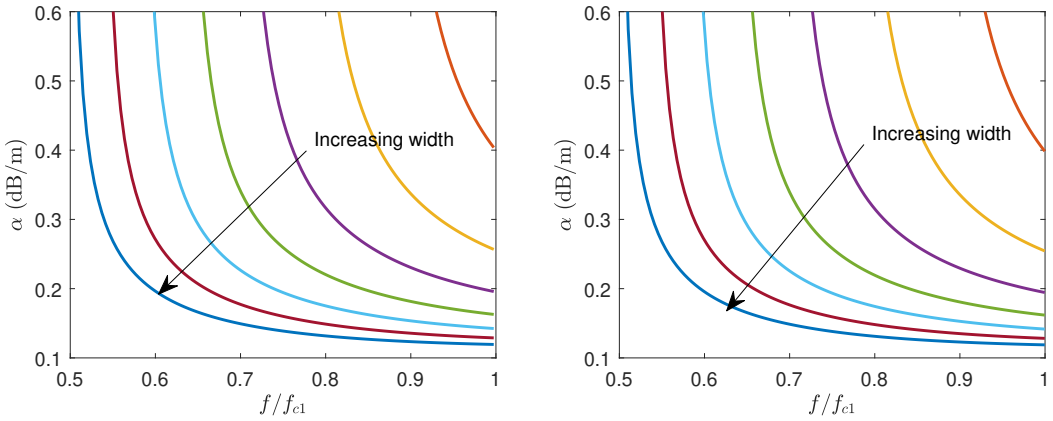

Figure 7.7: Attenuation constant for the cirgar waveguide: a) original cigar; b) cigar.

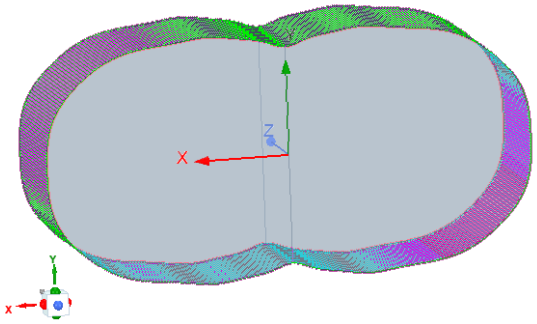

Figure 7.8: 3D model for the best potato waveguide in term of losses.

7.2.8 Best Smooth Walled Waveguides

It seems that the best frequency response in terms of insertion losses is achieved when the cross section of a waveguide family has the biggest surface (in width and height). Therefore, when higher order modes 1 and 2 are degenerated modes, which is also the case for the optimal result given by Suzuki and Hosono [5]. Fig. 7.10 permits the comparison between the best media in terms of losses for each of the smooth waveguide families. Also in this figure, a target which consists on a reduction of a 20% of the losses of the rectangular waveguide has been included in the plot (dashed-line in magenta). The analysis has been done in X-band. Despite of being irrelevant in simulation, the value of the cut-off frequency of the first higher

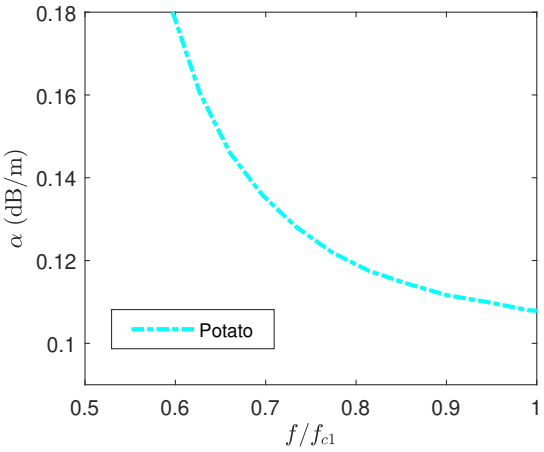

Figure 7.9: Attenuation constant for the potato waveguide.

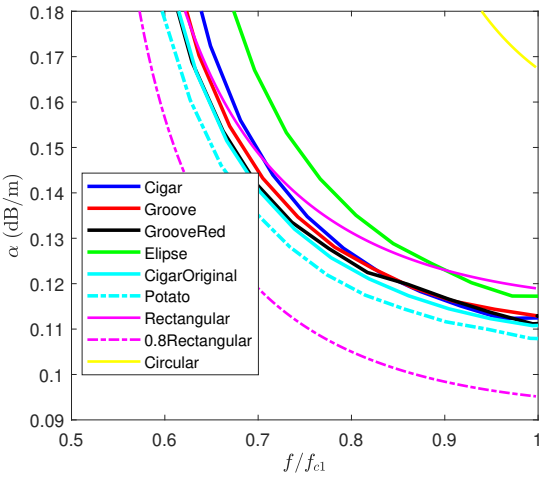

Figure 7.10: Comparison of several cross section in attenuation constant and bandwidth.

order mode should be taken into account in the manufacturing stage. Simulations have been carried out with high accuracy in order to make a fair comparison. Analyzing Fig. 7.10, it is clear that the best smooth waveguide is the potato, which achieves a losses reduction around 9% with respect to the rectangular one. However, as it has been commented previously, the manufacturing of a potato waveguide is very difficult, therefore, it is better to go into the original cigar waveguide which improvement in losses is around a 7%.

7.3 Periodic waveguides

When losses are a critical requirement, periodic waveguides are a classical design approach [7, 8]. However, the cross section optimization is not straight forward, hence transmission media are made with conventional shapes as rectangular, circular, etc. The losses reduction in the monomode band is not enough for the increase on complexity of the structures. Therefore, all of them are intended to be used in multimode band. Another approach consists on the use of smooth walled waveguides also in the multimode band where losses per unit length are small [6, 9, 10]. Both solutions, periodic and smooth walled waveguides, have a big inconvenient which is the possibility of multimode propagation. The excitation of several modes can be due to a discontinuity, for example in a bend, therefore, mode filters or mode convertors must be included in the routing, which increases losses and complexity [11].

This thesis explores a new option to reduce the losses of transmission media, which is the use of periodic waveguides but in monomode band with cross sections that have been optimized with this aim. In order to create the periodicity, the best cross-section from the smooth walled waveguide analysis has been chosen as a first guess to decrease the losses. Taking into account the degree of difficulty in the manufacturing process the original cigar shape has been chosen for the design. However, different periodic cross sections will be compared in order to support the fact that the best smooth waveguide is the one that produces the best periodic waveguide in terms of losses per unit length.

7.3.1 Simulation of Periodic Waveguides

This section details the analysis of low-loss periodic waveguides with commercial softwares. In previous chapters a general idea of simulating a periodic waveguide has been given, but when low-losses are considered, some precautions must be taken. Let us see, as an example of solution with HFSS, the analysis of a periodic waveguide formed with rectangular and cigar cross sections which will be called a compound period (more than two cross sections are involved), see Fig. 7.11a. The

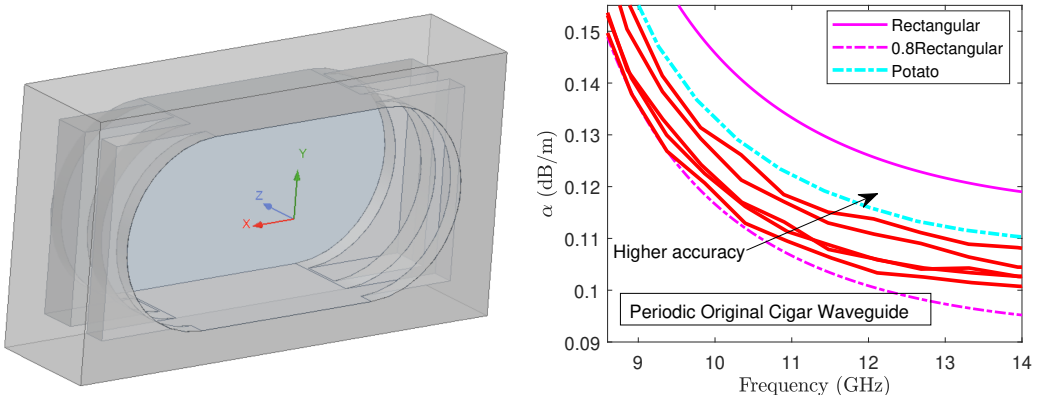

(a) **(b)**

Figure 7.11: Rectangular-cigar periodic waveguide: a) 3D model; b) HFSS simulation results.

attenuation constant is plotted in Fig. 7.11b in which the different red curves represent the results when the number of cells involved in the calculation of the electromagnetic field is increased (it is increased in different step sizes). A limitation in the number of cells along the simulations exists because of the finite computer memory, as well as the time of computation. Therefore, in this case, Fig. 7.11, it has not been possible to reach a converged solution. The lack of convergence happens for every complex waveguide that it is simulated. In order to get deep into the convergence problem, the simulation of two smooth waveguides: a circular and an elliptical with the same strategy as in the periodic waveguides has been carried out for different number of cells. The first cross section has an analytical solution for its attenuation constant. The elliptical's, on the contrary is based on the solution of a class of Mathieu's functions. Results for both waveguides are shown in Fig.7.12, and one can conclude that there is no difference in the results when the number of cells is increased. There is neither a difference between the results achieved by CST or HFSS (not shown here). Therefore, for both waveguides, the electromagnetic solution converges. So, a small value of losses is not the main problem, or at least a problem by itself, since the losses in Fig.7.12 are well estimated.

In order to see if the convergence problem is due to the internal sharp edges of periodic waveguides a second analysis has been carried out but this time with a smooth ridge waveguide. Fig. 7.13 shows the results. First, note that being the

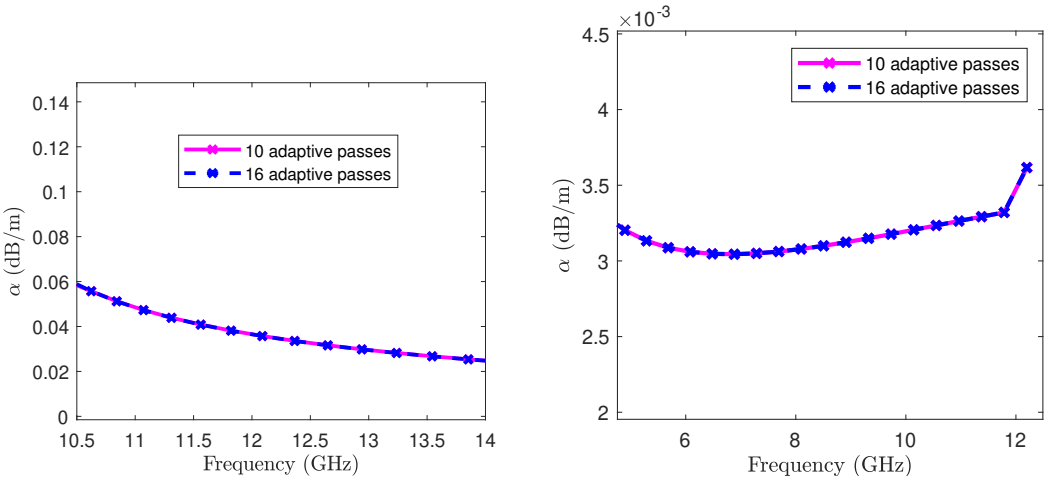

(a) **(b)**

Figure 7.12: HFSS simulation of the attenuation constant for: a) the TE_{01} mode of a circular waveguide; b) first higher order mode of an elliptical waveguide.

ridge waveguide smooth, a 2D solution can be executed. In that case, solutions with both softwares, HFSS and CST, rapidly converge when the mesh density is increased. Furthermore, the 3D analysis has been carried out using different canonical functions, results show that it is necessary to use the highest order (third order in both, CST and HFSS), but still there are high discrepancies between these results and the values given by a 2D solution. Therefore, the sharp edges have been smoothed by a small radius (5 μm in 20 mm), and the waveguide has been analyzed giving the results named rounded-edged in Fig. 7.13 for both commercial softwares. As it is shown, the convergence with CST and HFSS is possible when sharp-edges are smoothed since results equal the 2D solution. It can be concluded that sharp-edged structures do not let the adaptive mesh algorithm to converge or at least to converge fast enough for conventional computers. In Fig. 7.13b only the solutions that are considered converged are shown.

Let us now analyze a more complex and also more interesting transmission medium: a periodic cigar-elliptic waveguide (see Fig. 7.14). Let us see if both softwares manage to get the same solution when sharp edges are rounded. Fig. 7.15 shows the results of several analysis. First of all, it is straightforward to deduce that interior edges must be smoothed in order to get a converged solution when

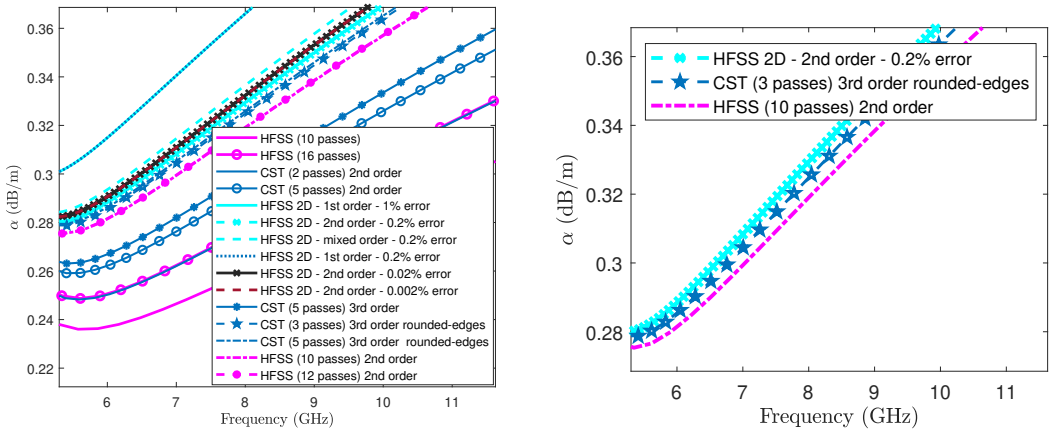

(a) **(b)**

Figure 7.13: Attenuation constant for the ridge waveguide: a) different analyses; b) zoom of the most accurate results.

using CST. Even if CST seems to have converged when a round-edged structure is computed, a measurement should be carried out to check that the convergence corresponds with the real value. In case of analyzing with HFSS, in none of the cases, smooth and sharp edges, a convergence is possible (the computer runs out of memory), but what it is more important: results are not even similar with CST's. Also in HFSS, two different mesh strategies have been applied: the curvilinear and the surface approximation, to see if there was any effect related. As Fig. 7.15 shows, both meshes give the same result. In summary, Fig. 7.15 shows that CST and HFSS do not reach the same result when sophisticated periodic waveguides are analyzed. It is possible to say that HFSS does not give a final result since it does not achieve a converged solution. Furthermore, it must be highlighted that in spite of achieving a converged solution with CST, there is nothing that can tell us if this result is the one corresponding to the geometry. Therefore, only the measurement of a waveguide can prove if CST converges to the right solution.

Let us see the different meshes in order to infer why results change so much when a small radius is included in the interior edges. Fig. 7.16 shows the effect on the mesh of rounding the internal edges. The small radius (5 μm in 20 mm) makes the mesh more dense in these locations to achieve the same convergence criteria (not really comparable since more cells are used when rounded edges are

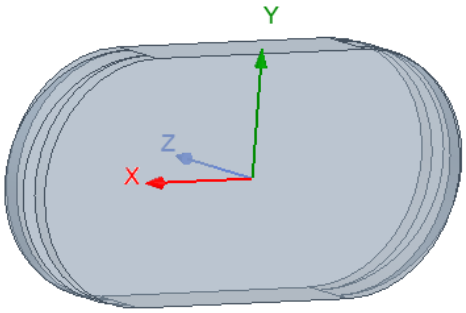

Figure 7.14: 3D model of a period of a cigar-elliptic waveguide.

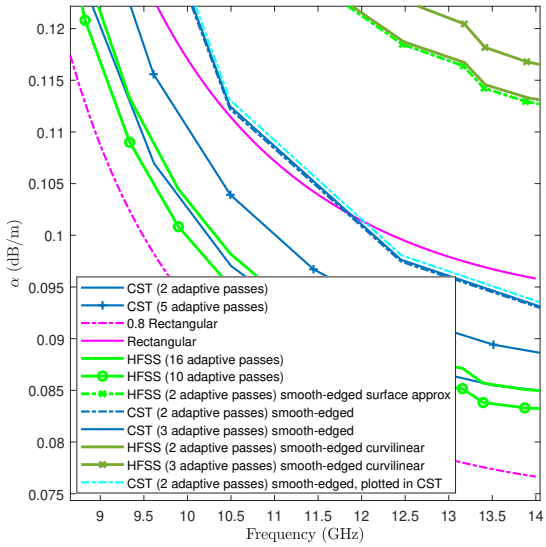

Figure 7.15: Attenuation constant of a cigar-elliptic waveguide.

analyzed). Therefore, it can be said that when sharp edges are simulated results are not accurate enough for the design of low-loss waveguides. This is because losses usually occur on that edges. Comparing the meshes in Fig. 7.16b and Fig. 7.16d, it can be concluded that using a surface approximation or a curvilinear mesh in HFSS gives different discretization of the geometry, but in both cases edges are the ones that are meshed the most. In case of analyzing with CST, a curvilinear mesh is internally used, as the warnings of the console states. Fig. 7.16c shows that also in this case the edges are meshed with a high density when they are rounded.

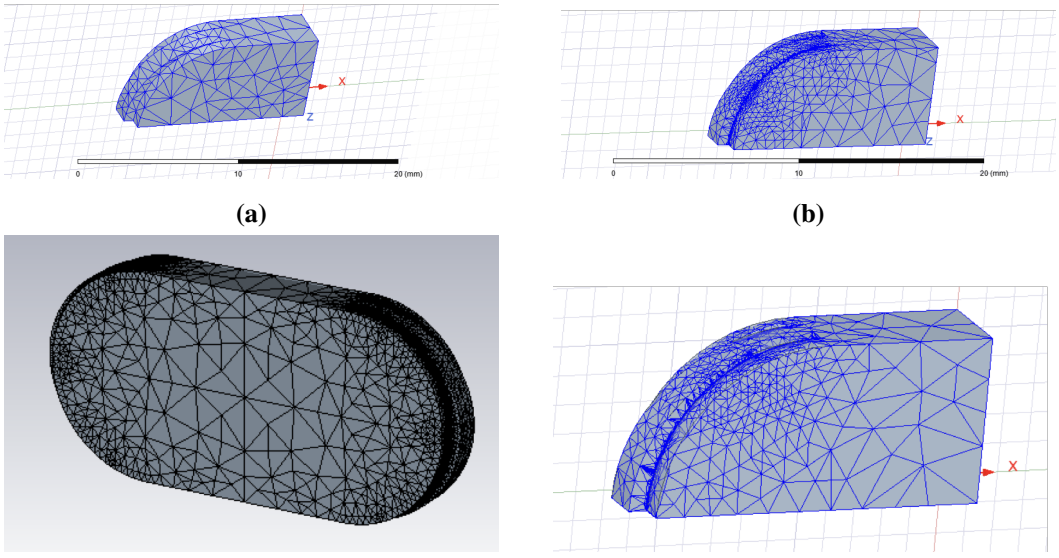

Figure 7.16: Meshes for a periodic cigar-elliptic waveguide: a) HFSS sharp edges; b) HFSS rounded edges, surface approximation mesh. c) CST rounded edges; d) HFSS rounded edges, curvilinear mesh.

Observing Fig. 7.16, it can be said that it is necessary to round the edges to get a mesh in accordance with the electromagnetic field variation. Besides, it seems that CST is able to achieve a higher mesh density (in all rounded edge structures the mesh density is increased until the computer runs out of memory). That could explain that in Fig. 7.15, only CST is able to give a converged solution, nonetheless no comparison with other softwares are possible. Therefore, only an experimental measurement could corroborate CST results.

7.3.2 Richardson Extrapolation

Previous sections showed that HFSS does not converge when complex structures are analyzed. In order to be able to achieve a convergence, an extrapolation to the limit of Richardson has been implemented. The technique is based on the hypothesis that the numerical error in the finite element method that estimates the electromagnetic field is proportional to the inverse of the number of cells used in the process. This is a rough approximation, but could be useful for our main ob-

jective, achieve a convergence. It is assumed that the second order basis functions is configured in HFSS. Therefore, the converged solution, r, is equal, when N cells have been used, to

$$r = r_N + \Theta\left(\frac{1}{N}\right) \tag{7.1}$$

where $\Theta(\frac{1}{N})$ represents the numerical error and where r_N is the finite element method electromagnetic field solution. The error can be rewritten in terms of the number of cells as an infinite sum:

$$r = r_N + \frac{k_1}{N} + \frac{k_2}{N^2} + \frac{k_3}{N^3} + ... \tag{7.2}$$

where k_i are unknown real constants. When the number of cells is increased the error is reduced, however, the computation time and the required computer memory increase a lot. Therefore, to reduce the numerical error, several simulations with different number of cells can be carried out, which gives a system of equations. For example if two simulations, with N_1 and N_2 number of cells, are carried out, then:

$$\begin{aligned} r &= r_{N_1} + \tfrac{k_1}{N_1} + \tfrac{k_2}{N_1^2} + \tfrac{k_3}{N_1^3} + ... \\ r &= r_{N_2} + \tfrac{k_1}{N_2} + \tfrac{k_2}{N_2^2} + \tfrac{k_3}{N_2^3} + ... \end{aligned} \tag{7.3}$$

Developing the previous system, the result can be expressed by

$$r = \frac{N_1 r_{N_1} - N_2 r_{N_2}}{N_1 - N_2} + k_2\left(\frac{-1}{N_1 N_2}\right) + k_3(...) + ... \tag{7.4}$$

So, now the biggest contribution of the error to the result is proportional to the inverse of the product of the number of cells used in both simulations. Two other simulations could be carried out to reduce the error to the product of the four number of cells. And, so on. Therefore it is possible to reduce the numerical error as much as the user wants. However, in order to get that, all simulations must be carried out equally spaced in the inverse of the number of cells that are used by the finite element method. This way, all combined errors are of the same magnitude.

Fig. 7.17 shows the compound periodic original cigar and rectangular waveguide that has been used to show how the extrapolation to the limit of Richardson

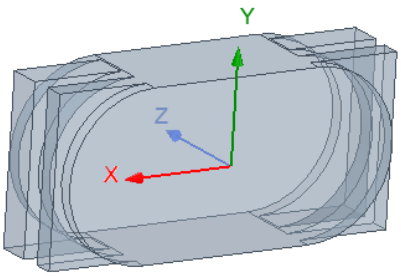

Figure 7.17: 3D model of the original cigar and rectangular compound periodic waveguide used for the implementation of the extrapolation to the limit of Richardson.

improves the convergence and decreases the computation time. In Fig. 7.18a several simulations with different number of cells for the waveguide have been plotted in red. Other curves like the smooth rectangular waveguide losses have been included as reference. Note that increasing the number of cells for the calculation makes this transmission medium to go from an improvement of nearly a 15% compared to the standard rectangular waveguide characteristics to become just better by around a 10%. Two groups of simulations have been designated and the Richardson limit calculated, results are shown in Fig. 7.18b in black traces. Two comments are necessary: first, it seems that results are very sensitive to the group designation; and second, Richardson results are more noisy than the actual simulations. If more groups are designated results can be worse as Fig. 7.19a shows. So, in order to see why Richardson results were getting that noisy, the resonant frequency of a period of the tranmsmission medium for the different number of cells simulations (curves in red in Fig. 7.19a) have been plotted as a function of the inverse of the number of cells in Fig. 7.19b. Note that in HFSS, convergence criteria is not achieved for the same number of cells for each frequency (phase delay in the periodic boundary).

Therefore, it has been stated that the number of cells should be the same for all frequencies. It has been fixed to the one necessary to achieved the convergence criteria at the middle of the monomode band. Results are shown in Fig.7.20. Note that now, the different simulations, plotted in black, are smoother, as well as the extrapolation result. Fig.7.20b shows that the number of cells are now constant with frequency. In Fig.7.20a, two different ways of calculating the extrapolation to the

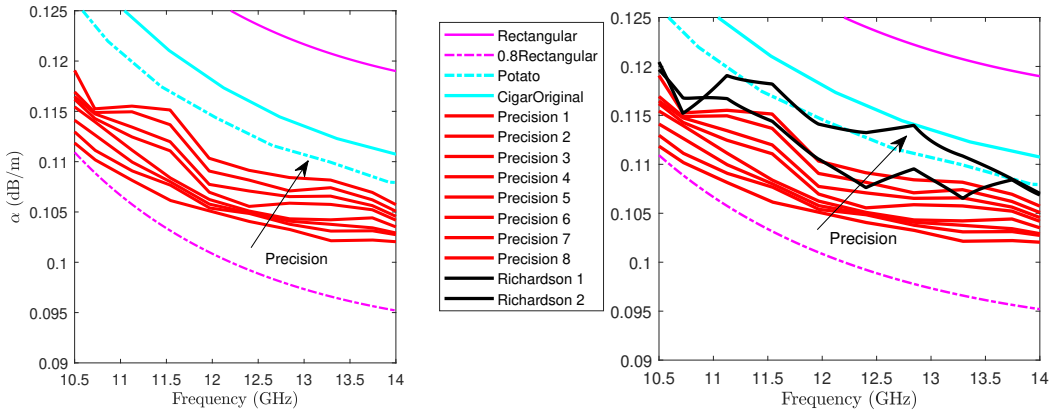

Figure 7.18: Attenuation constant for a compound periodic cigar-rectangular waveguide: a) HFSS results for different number of cells; b) Different results of the extrapolation to the Richardson limit by taking different sets of simulations.

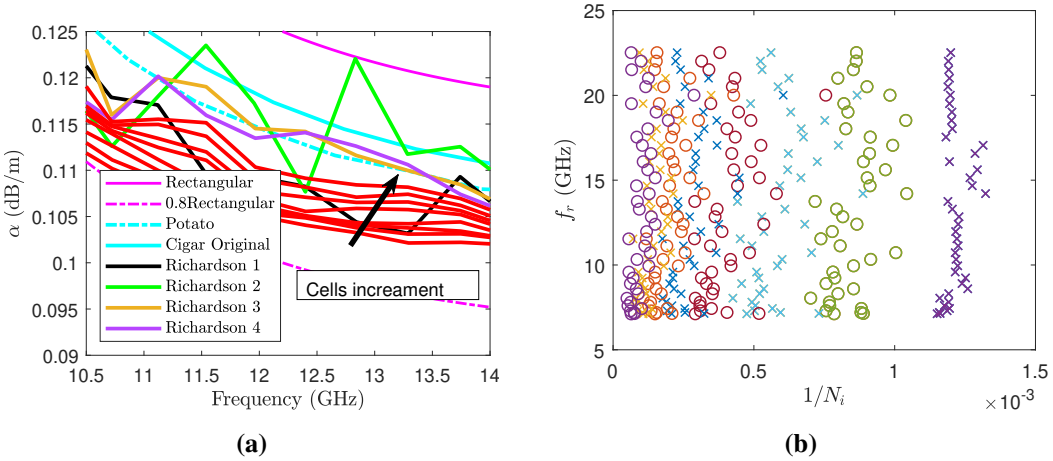

Figure 7.19: Attenuation constant for a compound periodic cigar-rectangular waveguide: a) HFSS results for different number of cells and Richardson results; b) Number of cells per frequency and simulation.

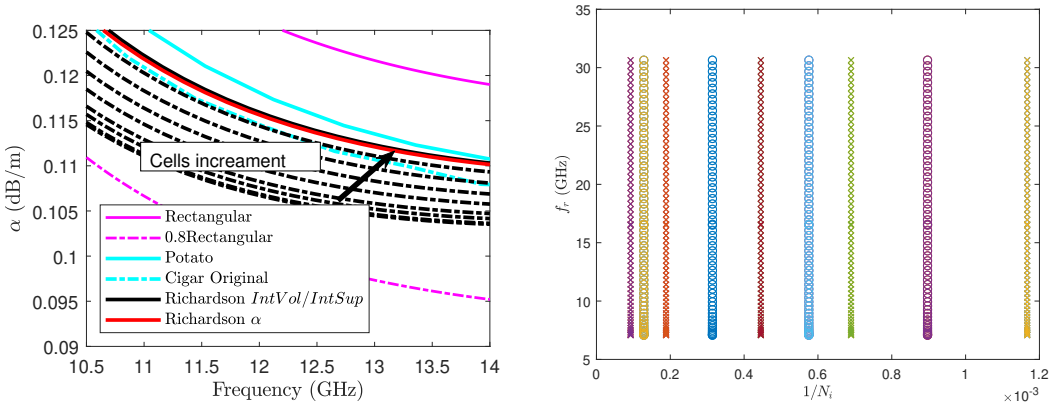

Figure 7.20: Attenuation constant for a compound periodic cigar-rectangular waveguide with the number of cells fixed in frequency: a) HFSS results for different number of cells and Richardson results; b) Number of cells per frequency and simulation.

limit of Richardson have been included. One is based on doing the extrapolation to the integrals of the magnetic field (needed in the calculation of the attenuation constant), and the other is based on applying the extrapolation directly to the attenuation constant. No differences are apreciable.

To sum up, the extrapolation permits to get rid of the numerical noise in finite element methods with no need of simulating with a high number of cells. It also increases the speed of convergence. However, note that the extrapolation to the limit of Richardson is only valid if the mesh adaptation varies monotonically, as well as the attenuation constant (an increase of the density of the mesh implies an increase of the losses and viceversa). Besides, it is very sensitive to the groups of simulations with which it is calculated, which means that a lot of simulations must be carried out to reduce the degree of dependence.

7.3.3 Gap Waveguides

Lately, a new kind of transmission medium has become very popular. They are usually called gap waveguides, ridge gap waveguides, mushroom waveguides... Let us include all of them in the family of gap waveguides. This section focuses on them since they have been defined as low-loss media. It will be shown that they

are not competitive in terms of losses compared to standard waveguides even when they are optimized on this aim.

These waveguides are based on a two periodic structure, one transversal and the other parallel to the wave propagation axis. They were firstly defined as a periodic two parallel plates medium [12]. Nonetheless, an infinite structure cannot be manufactured, so, only the infinite periodicity on the wave propagation axis has been maintained [1, 13, 14, 15, 16]. Besides, side walls have been added to the structure after three or four side periods to avoid radiation and interferences. This finite approximation and the inclusion of side walls work because the electromagnetic field is very small far from the centre plane of the structure. However, closing the side walls brings two problems. First, losses are increased, and second, two modes appear in the propagation band of the mode used in these media. Literature usually assumes that these new modes do not get excited, and therefore, it is not necessary to take them into account. However, here in this thesis, these two modes have been pushed out of the working band since low losses want to be reached. As the reader may know, the mode used in these media is not the fundamental, but a higher-order one, which is theoretically in a monomode band.

In Chapter 3, results of two gap waveguides have been discussed focusing on the algorithms and methods to analyze them. One of the transmission media being a conventional gap waveguide designed in X band, which 3D model has been repeated here for convenience, see Fig. 7.21. The other transmission medium, see Fig. 7.22, was the result of an optimization process of the latter waveguide cross section in unit-per-length losses with the requirement of not reducing the monomode operation. This section will explain the optimization process and will give a comparison in terms of losses with the most standard medium: the rectangular waveguide.

The initial gap waveguide is the result of a scaling process of the media that can be found in the technical literature. Its design it is basically based on designing the parallelepipeds to avoid the propagation of any mode in a pre-defined bandwidth, which has been fixed between 8 and 12 GHz. Then, the central channel, see Fig. 7.21, emulates (or can be assimilated to) a rectangular waveguide which is not closed abruptly. Therefore, the central channel dimensions are very similar to the ones of a rectangular waveguide in the desired propagation bandwidth (from

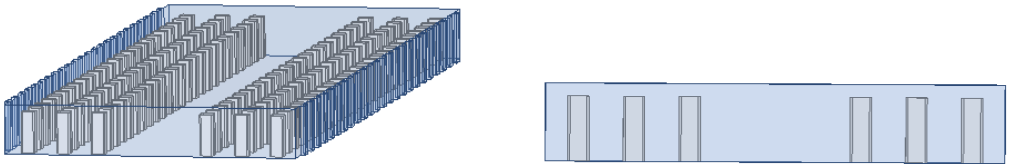

(a) **(b)**

Figure 7.21: A 3D model of the gap waveguide.

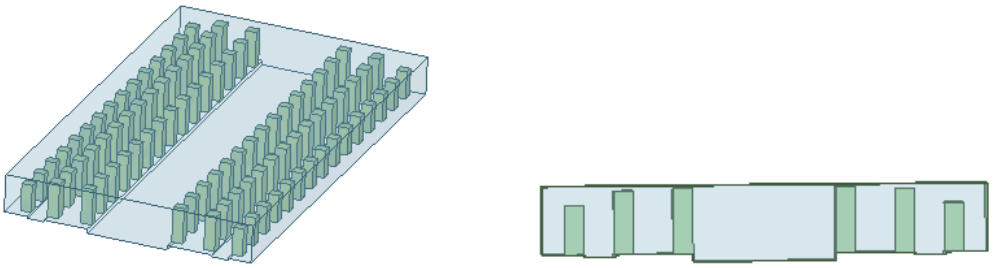

(a) **(b)**

Figure 7.22: A 3D model of the optimized gap waveguide.

8 to 12 GHz). Results of the design are shown in Fig. 7.23 under the name *Before optimization*. This geometry, has then been optimized with the aim to reduce the losses per-unit-length in the working bandwidth. The objective function is calculated in a wide range of frequencies, but only the values of the attenuation constant contained in the frequencies of interest are taken into account. In order to get a continuous objective function, when the minimum or the maximum mode frequency reduces the bandwidth a penalization value that increases exponentially with the bandwidth reduction has been included. In the working band the squared modulus of the attenuation constant is summed for all the frequencies. The resultant 3D model is shown in Fig. 7.22.

Results for both transmission media are shown in Fig. 7.23. Note that a reduction better than a 20% of the attenuation constant has been achieved by only letting the parallelepipeds to be different to each other. Also, in Fig. 7.23c the phase constant for several modes have been included to show that in the working band, from 8 to 12 GHz, both media are monomode. Finally, Fig. 7.23d shows the group velocity for the designed mode. It can be deduced from Fig. 7.23d that the attenuation constant has been reduced by increasing the quality factor of the medium instead of the other option that will be to decrease its dispersion. Only these two procedures are valid to decrease the losses of a medium as the general formulae for the attenuation constant states.

Fig. 7.24 shows the response of both gap waveguides, initial and optimized, for several algorithms and commercial softwares. Results of this figure have already been commented in Chapter 3, but it has been repeated here to show that commercial softwares do not have any convergence problems with this type of periodic waveguides.

To finish with this section, a comparison between the gap waveguide and the standard transmission media has been carried out. Fig. 7.25 shows the attenuation constant of the optimized gap waveguide of Fig. 7.22 together with its correspondent rectangular's. The latter means that the rectangular waveguide dimensions have been defined to have the cut-off frequency of its first higher order mode at 12.97 GHz, same value than for the optimized gap waveguide, see Fig. 7.23c. Results show that the optimized waveguide is very similar in terms of losses to the

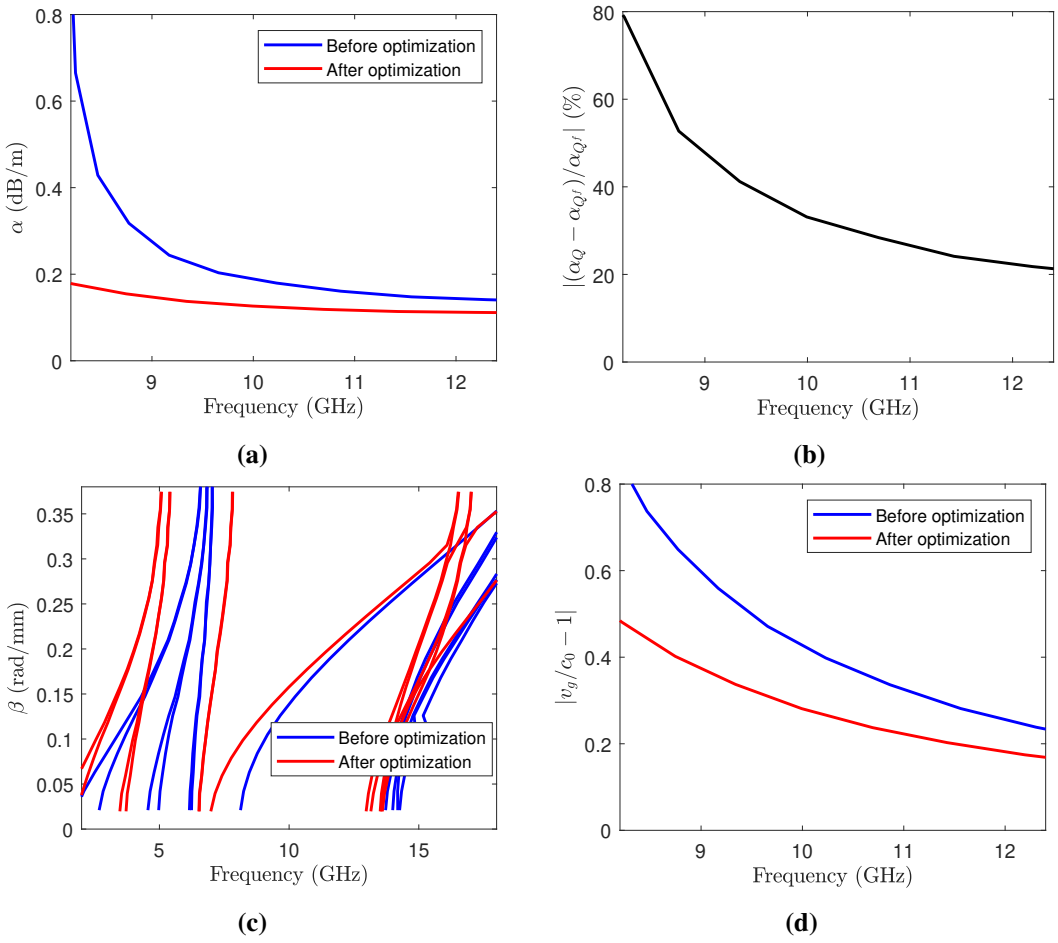

Figure 7.23: HFSS results for the gap waveguide before (Fig. 7.21) and after optimization (Fig. 7.22): a) Attenuation constant; b) Attenuation constant improvement; c) Phase constant; d) Group velocity.

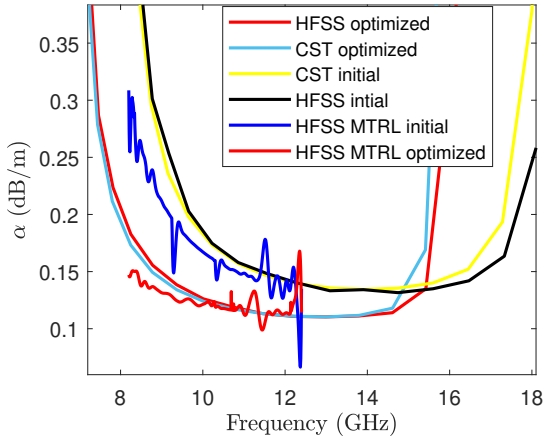

Figure 7.24: Algorithm comparison for the designed gap waveguides.

rectangular waveguide, however, if no optimization is carried out a difference bigger than a 20% will exist. It must be mentioned that one of the advantages of the gap waveguide is that it does not require a good connection between the side walls and the parallel plates since the field is concentrated in the central channel of the structure. Nonetheless, in Section 7.2.8 it has been shown that the cigar waveguide permits and improvement of the rectangular waveguide near a 7%. Therefore, the difference between the attenuation constant of a cigar waveguide and the optimized waveguide are higher than a 10%. If the structures are designed above Ka band and they need to be manufactured in several pieces a comparison between the losses that arise from manufacturing the cigar in two pieces (cut through its central plane, in which currents are zero) and the gap waveguide manufactured in four pieces (parallel plates with the parallelepipeds and side walls) should be carried out. Under my point of view, I do not think losses will rise more than a 10% in the cigar waveguide because of that cut. Therefore, it seems that the cigar waveguide is more advantageous in a low-loss environment. Besides, it is much faster and easy to manufacture than an optimized gap waveguide.

7.3.4 Low-Loss Solutions

Along this thesis, different cross sections have been studied with the aim of reducing the losses per unit length of the transmission media. In Section 7.2 differ-

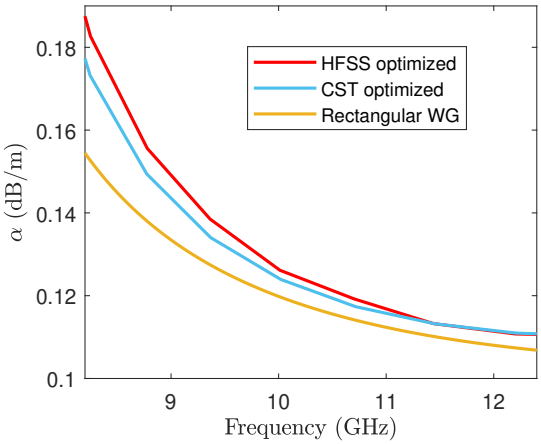

Figure 7.25: Comparison of the optimized gap waveguide with the correspondent rectangular waveguide (same next higher order mode cut-off frequency).

ent smooth waveguides have been analyzed and compared. Taking into account the degree of difficulty of the cross section, as well as the losses, several periodic waveguides have been formed. The most promising is without any doubt the cigar periodic waveguide that is shown in Fig. 7.26. Also in this figure, the optimization parameters have been depicted. Despite of knowing that the two higher order modes must be degenerated in order to get the lowest losses, several structure could produce this phenomena. Therefore, an optimization has been mandatory. CST results are shown in Fig. 7.27, however, it must be noted that convergence to the right value in complex structure like this one have not been proven (HFSS is not even able to converge). In this simulation, for sure, the $5\ \mu m$ edges-radius has been included. As Fig. 7.27 shows, this transmission medium seems promising in terms of losses since it achieves an amelioration of a $20\ \%$ compared to the best manufacturable equivalent smooth rectangular waveguide. However, it must be noted that this solution is not reliable since when more cells are included in the simulation, the losses are higher as Fig. 7.15 shows. Only the measurement of this transmission medium will give the real value of its attenuation constant.

Nonetheless, milling workshops were not able to manufacture it, or they gave very high quotations, which also made impossible its manufacturing. A workshop that combines 3D printing with milling finally accepted its manufacturing but to

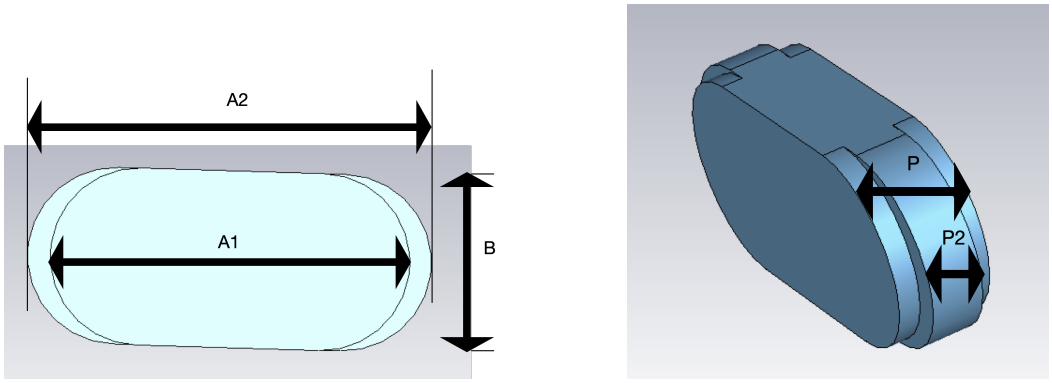

(a) **(b)**

Figure 7.26: 3D model that includes the optimization parameters of a cigar original - cigar elliptical waveguide: a) front view; b) side view.

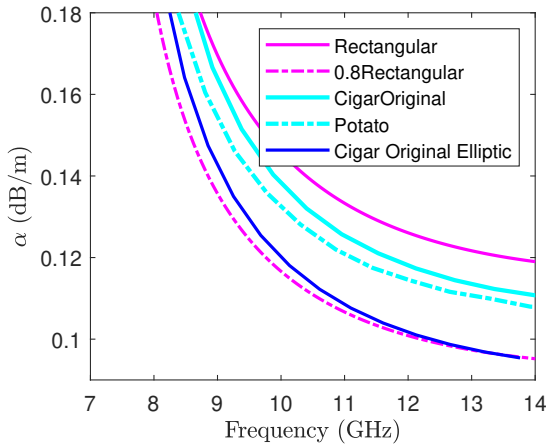

Figure 7.27: Comparison in CST of the optimized periodic original and elliptic cigar waveguide with its equivalent rectangular waveguide (same higher order mode cut-off frequency).

the date it has not been finished. Other structures have been analyzed with the aim to simplify the geometry for a milling process by changing the elliptic cigar part by grooves, Fig. 7.28 shows the 3D model. And the results of its attenuation constant estimation, once the parameters have been optimized, are depicted in Fig. 7.29 together with the main smooth waveguides we are comparing to. HFSS estimates the transmission medium better than a cigar waveguide, but the improvement, by a

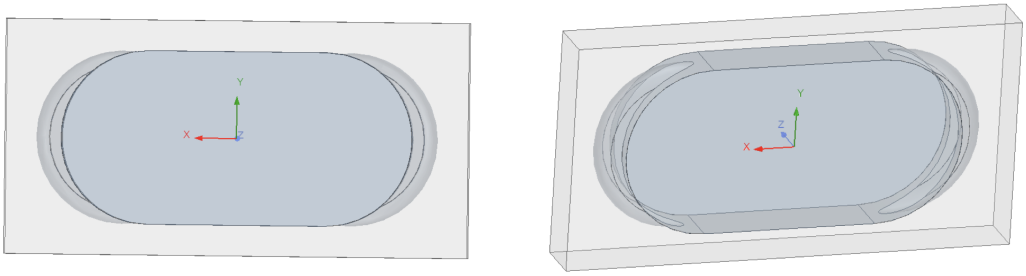

(a) **(b)**

Figure 7.28: 3D model of a cigar original - elliptical rounded waveguide: a) front view; b) side view.

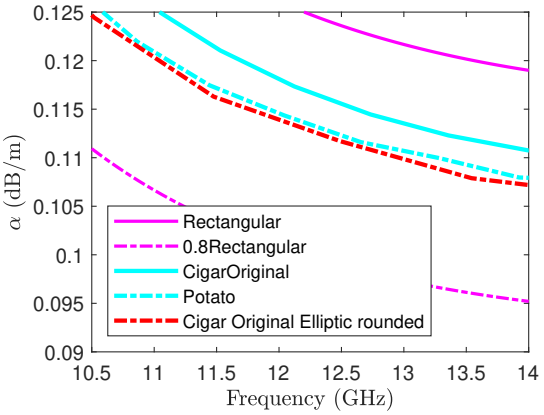

Figure 7.29: Comparison in HFSS of the optimized periodic original and elliptic cigar waveguide rounded with its equivalent rectangular waveguide (same higher order mode cut-off frequency).

3% from a smooth cigar waveguide, is not enough to justify the complexity of the structure.

Therefore, the grooves have been changed by a rectangular shape, see Fig. 7.30 to check the 3D model. HFSS estimates the transmission medium better than a cigar waveguide by a 6% in unit-per-length losses compared to a smooth cigar waveguide, see Fig. 7.29. Again, the improvement does not seem to justify the increase on complexity of the transmission medium structure.

Not being able to reduce the unit-per-length losses to the target of a 20% of the smooth rectangular's, a waveguide with a compound period has been analyzed. The

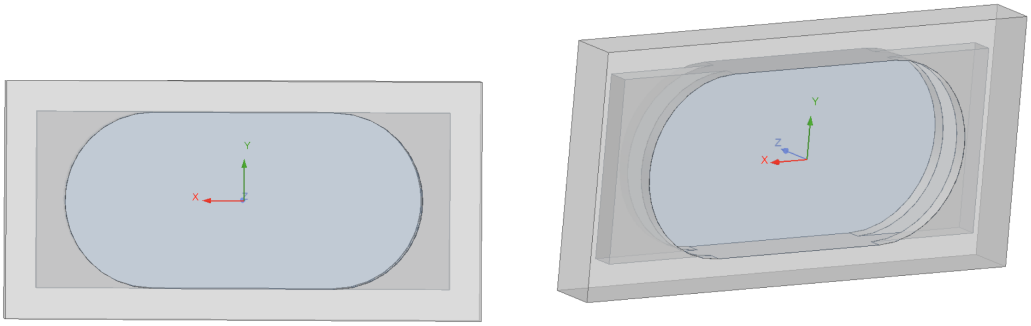

(a) **(b)**

Figure 7.30: 3D model of a cigar original - rectangular waveguide: a) front view; b) side view.

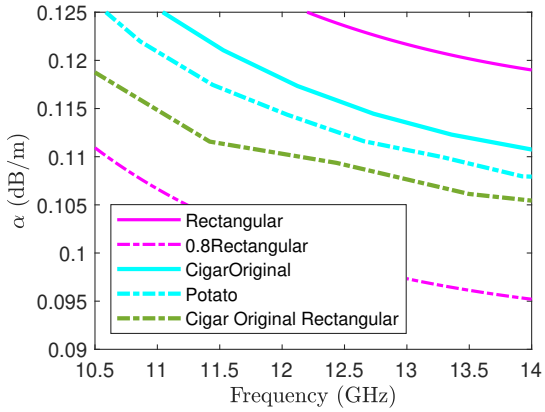

Figure 7.31: Comparison in HFSS of the optimized periodic original cigar and rectangular waveguide with its equivalent rectangular waveguide (same higher order mode cut-off frequency).

transmission medium is a cigar original waveguide with two periods of different rectangular shapes as Fig. 7.32 shows. In the left the initial structure is shown, and in the right a feasible structure by a milling tool is depicted. In Fig. 7.33 the attenuation constant has been included for the manufacturable medium by milling. It can be seen that results are far from the defined target.

It must be commented that all the results shown in this section are not reliable until some measurement are carried out. However, they have been included here because they seem all better than a conventional rectangular waveguide. But,

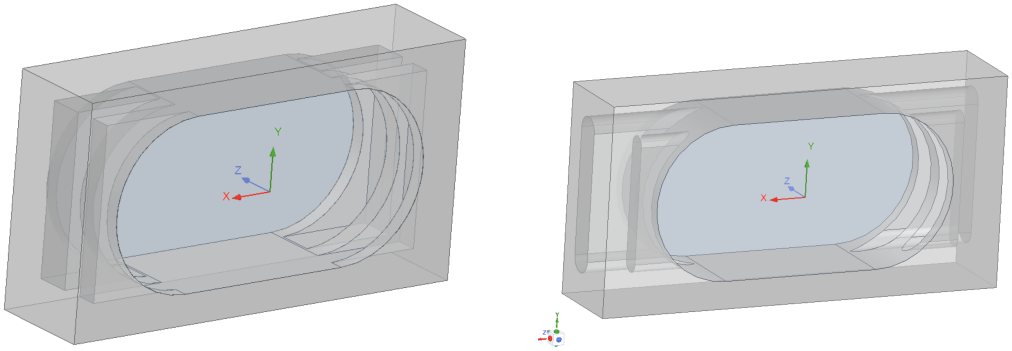

(a) (b)

Figure 7.32: 3D model of a compound waveguide with cigar original - rectangular cross sections: a) sharp edged; b) feasible structure by milling.

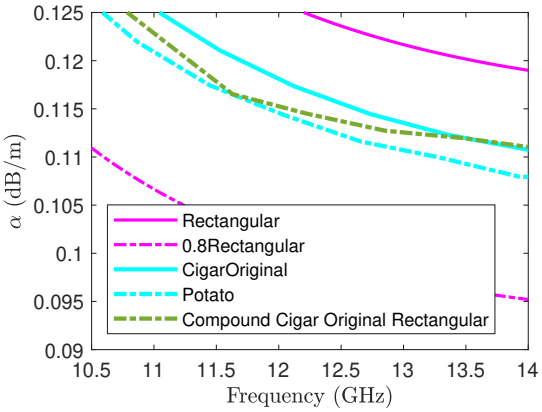

Figure 7.33: Comparison in HFSS of the optimized compound period original cigar and rectangular waveguide with its equivalent rectangular waveguide (same higher order mode cut-off frequency).

what does not seem clear is if the complexity that involves the manufacturing of a periodic medium worths the reduction on losses per-unit-length they imply.

7.4 Conclusions

This chapter has firstly defined a comparison criterium between transmission media, and then the smooth waveguides have been analyzed. It has been shown that

the smooth waveguide problem had already been solved with the potato waveguide. However, if losses need to be reduced even more, then two options are possible. First, to work in the multimode band, which reduces the unit-per-length losses but does not really reduce the overall system's losses because of the excitation of other modes and the need for mode suppressors. Second, to make the waveguides periodic. This chapter has been devoted to the analysis and design of periodic waveguides, showing that they are a promising transmission medium. However, commercial software still have some trouble to estimate their characteristics because of the numerical noise. It is hoped, that in the future this noise will be overcome by the improvement of the numerical methods or by the power of the computer's memory. Meanwhile, some measurements must be carried out to get a real estimation of the losses of periodic media with complicated cross sections.

References

[1] P.-S. Kildal, E. Rajo-Iglesias, E. Alfonso, A. Valero, and A. U. Zaman, "Wideband, lowloss, low-cost, quasi-tem metamaterial-based local waveguides in air gaps between parallel metal plates," in *2009 International Conference on Electromagnetics in Advanced Applications*, 2009, pp. 588–591. 204, 222

[2] E. Pucci, A. U. Zaman, E. Rajo-Iglesias, P.-S. Kildal, and A. Kishk, "Losses in ridge gap waveguide compared with rectangular waveguides and microstrip transmission lines," in *Proceedings of the Fourth European Conference on Antennas and Propagation*, 2010, pp. 1–4. 204

[3] A. M. B. Al-Hariri, "Low attenuation microwave waveguides," Ph.D. dissertation, Queen Mary, University of London, 1974. 207

[4] G. Bartolucci and G. Leuzzi, "Loss and bandwidth considerations in closed groove waveguides," in *1987 17th European Microwave Conference*, 1987, pp. 940–944. 207

[5] M. Suzuki and T. Hosono, "Optimum sectional shape of dominant mode waveguide," *IEEE Transactions on Microwave Theory and Techniques*, vol. 31, no. 10, pp. 836–841, 1983. 208, 209, 210

[6] U. Rosenberg, T. Sieverding, R. Beyer, H. Höfers, F. Bodendieck, H. Segelke, S. Ptacek, K. M. Vögerl, and M. P. Andreas Raith, "Bundled waveguide harness for multibeam satellites," Mician Global Engineering GbR, OHB AG,Rohde&Schwarz GmbH & Co. KG, Tech. Rep., 2017. 209, 212

[7] A. Al-Hariri, A. Olver, and P. Clarricoats, "Low-attenuation properties of corrugated rectangular waveguide," *Electronics Letters*, vol. 10, pp. 304–305(1), July 1974. [Online]. Available: https://digital-library.theiet.org/content/journals/10.1049/el_19740241 212

[8] P. Clarricoats and P. Saha, "Attenuation in corrugated circular wave-guide," *Electronics Letters*, vol. 6, pp. 370–372(2), June 1970. [Online]. Available: https://digital-library.theiet.org/content/journals/10.1049/el_19700260 212

[9] H. Butterweck and F. de Ronde, "Oversized rectangular waveguide components for mm waves," in *1967 G-MTT International Microwave Symposium Digest*, 1967, pp. 35–38. 212

[10] U. Rosenberg and M. Schneider, "High-performance transitions for overmoded operation of elliptical waveguides," *IEEE Transactions on Microwave Theory and Techniques*, vol. 48, no. 10, pp. 1749–1755, 2000. 212

[11] A. Fontana and B. Lazareff, "Alma memo no. 550," Institut de RadioAstronomie Millimétrique, Tech. Rep., 2006. 212

[12] P.-S. Kildal, "Waveguides and transmission lines in gaps between parallel conducting surfaces," European Patent EP08 159 791.6, July 7th, 2008. 222

[13] A. T. Domínguez, J. F. González, J. I. Alonso, and M. Sierra-Pérez, "Design proposal for ridge gap waveguide and comparison with other technologies in ka to w bands," in *2016 10th European Conference on Antennas and Propagation (EuCAP)*, 2016, pp. 1–5. 222

[14] A. Tamayo-Domínguez, J.-M. Fernández-González, and M. Sierra-Pérez, "Groove gap waveguide in 3-d printed technology for low loss, weight, and cost distribution networks," *IEEE Transactions on Microwave Theory and Techniques*, vol. 65, no. 11, pp. 4138–4147, 2017. 222

[15] A. Tamayo-Domínguez, J.-M. Femández-González, and M. Sierra-Pérez, "Low losses printed distribution network technologies for planar antennas in ka band," in *2017 11th European Conference on Antennas and Propagation (EUCAP)*, 2017, pp. 3147–3151. 222

[16] A. Berenguer, V. Fusco, D. E. Zelenchuk, D. Sánchez-Escuderos, M. Baquero-Escudero, and V. E. Boria-Esbert, "Propagation characteristics of groove gap waveguide below and above cutoff," *IEEE Transactions on Microwave Theory and Techniques*, vol. 64, no. 1, pp. 27–36, 2016. 222

CHAPTER

8

Conclusions and Perspectives

8.1 Conclusions

The main objective of this tesis is to contribute to the reduction of losses between satellite communication modules. After the high power amplifiers, the interconnections are done with standard waveguides, which losses increase with the operation frequency. As it has been mentioned the systems' frequency is being increased to reach higher data rates. Therefore, the design of a waveguide with lower losses than the standard's is of main interest. The proposal of this thesis is the design of monomode periodic waveguides, which seems promising to reduce losses without decreasing the operational bandwidth significantly.

- *Advanced designs*: For the first time, it has been presented a rigorous procedure to design monomode asymmetric devices in which half of it is K times the other half. The presented design method gives not only new possibilities to the power distribution of any network including measurement set ups, but also, a design starting point for the design of multiport devices. Coupled-line couplers, branch-line couplers and a six-port power divider have been designed and manufactured, results show that the method is accurate and it even permits to avoid the conventional optimization step.

Also, the design of mode launchers based on couplers has been included. The design procedure permits a great flexibility to choose the modes to be excited at the output port. The result of these designs has its importance in the measurement field, since set ups are usually formed with this kind of devices as it has been the case in this thesis for multimode measurements.
Finally, low-loss periodic waveguides have been designed and analyzed. Improvements in losses compared to their equivalent rectangular waveguide have been achieved and are around a 15 %. The main idea of the designs has been to modify the waveguides' cross section through an optimization program, which aim was to reduce the attenuation constant of the periodic media.

- *Advanced simulations*: This thesis includes an intensive review of different strategies that permit to get the attenuation constant of any transmission medium with comercial software packages. The novelty, is the ability to use them to characterize periodic waveguides. To do it, the relationship between the attenuation constant and the quality factor of a closed non TEM transmission medium has been reviewed. Finite element full-wave electromagnetic programs have been chosen for the task of this thesis because there is no constraint on the geometry to be simulated. However, it has been found that internal edges increase the numerical noise, and therefore, the analysis can become unable to converge. With that on mind, the design strategy to get low losses from an intensive review of smooth waveguides characteristics has been given. Several final designs that improve rectangular waveguides results have been included. Finally, gap waveguides have also been analyzed and optimized in terms of losses and bandwidth since they can be considered periodic media. An accurate simulation of their characteristics is given in this thesis.

- *Advanced measurements*: A great effort in the measurement of low-loss transmission media has been carried out all along this thesis. Both monomode and multimode media have been considered. It has been presented for the

first time here in this thesis an accurate multimode vector network analyzer calibration, as well as the measurement method to characterized accurately multimode transmission media. Furthermore, an intensive review of the measurement methods to get the propagation constant have been included and their characteristics discussed and compared. Also, quality factor measurement methods have been discussed in one of the chapters of this thesis. With the obtained formula that relates the quality factor to the attenuation constant, it has been possible to use these methods to characterize any monomode transmission medium. As a general conclusion for the quality factor measurements, it can be commented that long resonator sections must be considered.

8.2 Future Research Lines

The main topic of this thesis: *design of low-loss periodic transmission media with the aim of reducing its rectangular equivalent waveguide losses in a* 20 *% without loosing bandwidth significantly* has been very ambitious. And therefore, several lines of research should be carried out in order to complete it. The work that should be carried out can be divided into three topics:

1. Long sections of different transmission media (a smooth rectangular waveguide, a smooth ridge waveguide, and several periodic waveguides) should be manufactured with the same procedure and their measurement characterization should be compared to the simulation estimations.

2. Issues related to high power periodic transmission media should be studied.

3. Development of complex waveguide routing with bends, twists, transitions, should be carried out and then manufactured and tested.

Furthermore, several topics regarding the design of advanced microwave devices that could be developed are:

1. To develop the circuit theory to design asymmetric devices without constrains.

2. To use the asymmetric branch line theory design presented in this thesis for the design of orthomode transducers.

3. To design, relying on the coupling matrix filter's theory, asymmetric branch lines using the other symmetry compared to the one presented here.